

No evidence of AGN features in the nuclei of Arp 220 from JWST/NIRSpec IFS

Michele Perna^{1*}, Santiago Arribas¹, Isabella Lamperti¹, Miguel Pereira-Santaella², Lorenzo Ulivi^{3,4,5}, Torsten Böker⁶, Roberto Maiolino^{7,8,9}, Andrew J. Bunker¹⁰, Stéphane Charlot¹¹, Giovanni Cresci⁴, Bruno Rodríguez Del Pino¹, Francesco D'Eugenio^{7,8}, Hannah Übler^{7,8}, Katja Fahrion¹², and Matteo Ceci^{3,4}

¹ Centro de Astrobiología (CAB), CSIC-INTA, Cra. de Ajalvir Km. 4, 28850 – Torrejón de Ardoz, Madrid, Spain

² Instituto de Física Fundamental, CSIC, Calle Serrano 123, 28006 Madrid, Spain

³ Università di Firenze, Dipartimento di Fisica e Astronomia, via G. Sansone 1, 50019 Sesto F.no, Firenze, Italy

⁴ INAF - Osservatorio Astrofisico di Arcetri, Largo E. Fermi 5, I-50125 Firenze, Italy

⁵ University of Trento, Via Sommarive 14, I-38123 Trento, Italy

⁶ European Space Agency, c/o STScI, 3700 San Martin Drive, Baltimore, MD 21218, USA

⁷ Kavli Institute for Cosmology, University of Cambridge, Madingley Road, Cambridge, CB3 0HA, UK

⁸ Cavendish Laboratory - Astrophysics Group, University of Cambridge, 19 JJ Thomson Avenue, Cambridge, CB3 0HE, UK

⁹ Department of Physics and Astronomy, University College London, Gower Street, London WC1E 6BT, UK

¹⁰ Department of Physics, University of Oxford, Denys Wilkinson Building, Keble Road, Oxford OX1 3RH, UK

¹¹ Sorbonne Université, CNRS, UMR 7095, Institut d'Astrophysique de Paris, 98 bis bd Arago, 75014 Paris, France

¹² European Space Agency, European Space Research and Technology Centre, Keplerlaan 1, 2201 AZ Noordwijk, the Netherlands

March 22, 2024

ABSTRACT

Context. Arp 220 is the nearest ultra-luminous infrared galaxy; it shows evidence of 100 pc-scale molecular outflows likely connected with galaxy-scale outflows traced by ionised and neutral gas. The two highly obscured nuclei of Arp 220 are the site of intense star formation, with extreme (far-infrared based) star-formation rate surface densities, $\Sigma_{SFR} \gtrsim 10^3 \text{ M}_\odot \text{ yr}^{-1} \text{ kpc}^{-2}$. Despite extensive investigations searching for active galactic nucleus (AGN) activity in the Arp 220 nuclei, direct evidence remains elusive.

Aims. We present JWST/NIRSpec IFS observations covering the 0.9 – 5.1 μm wavelength range of the innermost ($5'' \times 4''$, i.e. $1.8 \times 1.5 \text{ kpc}$) regions of Arp 220. The primary goal is to investigate the potential presence of AGN signatures in the nuclear regions by analysing the spectra extracted from circular apertures of radius 55 pc ($0.15''$) around each of the two nuclei.

Methods. The analysis aims to identify highly ionised gas emission lines (with ionisation potential $> 54 \text{ eV}$) and other spectral features indicative of AGN activity. Ionised and molecular gas kinematics are also taken into account to study the outflow signatures at $< 60 \text{ pc}$ scales.

Results. We identify ~ 70 ionised and ~ 50 molecular emission lines in the nuclear spectra of Arp 220. We use recombination line ratios to measure optical extinctions in the range $A_V \sim 11 - 14 \text{ mag}$. High ionisation lines are not detected, except the [Mg IV] line at $4.49 \mu\text{m}$ which we interpret as due to shocks rather than to AGN ionisation. We identify broadening and multiple kinematic components in the H I and H₂ lines caused by outflows and shocks, with velocities up to $\sim 550 \text{ km s}^{-1}$. Significantly higher velocities (up to $\sim 900 \text{ km s}^{-1}$) are detected in the off-nuclear regions; however, they do not conclusively represent evidence for AGN activity.

Conclusions. Even with the unprecedented sensitivity of JWST/NIRSpec IFS, achieving an unambiguous identification or exclusion of the presence of an AGN in the Arp 220 system remains challenging, because of its extreme dust obscuration.

Key words. galaxies: individual: Arp 220 – galaxies: active – galaxies: starburst – galaxies: ISM

1. Introduction

Arp 220 is the closest ultra-luminous infrared galaxy (ULIRG), with a distance of $\sim 78 \text{ Mpc}$ and $\log L_{IR}/L_\odot = 12.2$ (e.g. Pereira-Santaella et al. 2021). This late-stage merger shows several tidal structures in the outskirts (e.g. Arp 1966; Arribas et al. 2001; Perna et al. 2020) and contains two compact ($< 150 \text{ pc}$), highly obscured nuclei separated by $\sim 370 \text{ pc}$ ($1''$) that dominate the infrared luminosity (e.g. Scoville et al. 2007).

The nuclear region of Arp 220 is the site of an intense star formation, with a star formation rate $SFR \sim 200 - 250 \text{ M}_\odot \text{ yr}^{-1}$ (e.g. Nardini et al. 2010; Varenus et al. 2016) and incredibly high star formation rate surface densities ($\Sigma_{SFR} \sim 10^3 - 10^4$

$\text{M}_\odot \text{ yr}^{-1} \text{ kpc}^{-2}$, from radio and far-infrared observations; e.g. Barcos-Muñoz et al. 2015; Pereira-Santaella et al. 2021). Long-term monitoring with very long baseline interferometry has revealed dozens of supernovae and supernova remnants resulting from the extreme star formation occurring in the compact nuclei (e.g. Varenus et al. 2019). The off-nuclear regions appear to have post-starburst properties, with weak star formation produced in a few young and low-mass clusters (e.g. Perna et al. 2020; Chandar et al. 2023), as expected for a late-stage merger.

Although Arp 220 has been extensively studied from radio to hard X-ray and γ -ray wavelengths, there is still no convincing direct evidence for the presence of active galactic nucleus (AGN) activity in either of the two nuclei; however, indirect arguments provide suggestive indications (e.g. Teng et al. 2015; Paggi et al. 2017; Yoast-Hull & Murray 2019). Accreting super-

* e-mail: mperna@cab.inta-csic.es

massive black holes (SMBHs) could be buried in Compton-thick absorbers (i.e. $N_H > 1.5 \times 10^{24} \text{ cm}^{-2}$) at the position of the two nuclei (Teng et al. 2015; Sakamoto et al. 2021a) and, for instance, explain the excess of γ -ray flux in comparison to all other diagnostics of star-forming activity (Yoast-Hull et al. 2017).

Evidence of multi-phase (i.e. molecular, neutral, and ionised) outflows in Arp 220 have been inferred from the analysis of multi-wavelength observations. Collimated outflows have been discovered in both nuclei on scales of ~ 100 pc using, for instance, ALMA observations of carbon monoxide transitions (e.g. Wheeler et al. 2020; Ueda et al. 2022; Lamperti et al. 2022); large-scale outflows have also been identified with optical integral field instruments (IFS; e.g. Arribas et al. 2001; Colina et al. 2004; Perna et al. 2020) and associated with extended soft X-ray emission (e.g. McDowell et al. 2003). The possible connection between these multi-phase and multi-scale outflows has not yet been investigated in detail. Consequently, the mechanisms at the origin of these outflows, and hence whether they are due to starburst or AGN winds, are still debated.

In this work, we revisit Arp 220 and its nuclear regions taking advantage of JWST observations performed with the IFS unit of the NIRSpec instrument (Jakobsen et al. 2022; Böker et al. 2022); these data cover the near-infrared (NIR) wavelength range between 0.95 and 5.1 μm . The observations were taken as part of the JWST/NIRSpec IFS Guaranteed Time Observations (GTO) survey “Resolved structure and kinematics of the nuclear regions of nearby galaxies” (program lead: Torsten Böker). The analysis presented in this paper aims to identify AGN signatures in the Arp 220 nuclei, as the presence of highly ionised gas and extreme kinematics unambiguously associated with accreting SMBHs.

The rest of this paper is organised as follows. Section 2 presents the NIRSpec IFS observations and data reduction. Section 3 describes the spectral fitting analysis and the identification of emission line species. Section 4 reports a qualitative description of the nuclear spectra as well as that of a nearby bright stellar cluster, and some general properties of the interstellar medium (ISM). The multi-phase outflow properties, the absence of highly ionised species, and the comparison between H I and far-IR SFR tracers are discussed in Section 5. Finally, Section 6 summarises our conclusions. Throughout this work, we assume $\Omega_m = 0.286$ and $H_0 = 69.9 \text{ km/s/Mpc}$ (Bennett et al. 2014). With this cosmology, 1'' corresponds to a distance of 0.368 kpc at $z = 0.018$.

2. Observations and data reduction

Arp 220 was observed in NIRSpec IFS mode as part of the programme 1267 (PI: D. Dicken). The present observations were combined in a single proposal with independent MIRI acquisitions of the same target, with the aim of saving the telescope slew overhead. The observations were collected on 6 March 2023, using the NIRSpec IFS mode (Böker et al. 2022).

The dataset consists of two distinct sets of four-point medium cycling dithering pattern with 15 groups per exposure. The first set is centred at the mid-point between the coordinates of the western (W) and the eastern (E) nuclei; the second set is offset $\sim 1''$ towards the north-west to cover the shell of H α and [N II] emission (e.g. Lockhart et al. 2015; Perna et al. 2020). The total integration time is 933 seconds per set, in each of the three high resolution (R ~ 2700) grating settings, to cover the spectral range from 0.95 to 5.1 μm .

2.1. Data reduction

We used the STScI pipeline v1.8.2 with CRDS context 1063. A patch was included to correct some important bugs that affect this specific version of the pipeline (see details in Perna et al. 2023). In particular, we corrected the count-rate images for $1/f$ noise by fitting a polynomial. During stage 2, we masked pixels at the edge of the slices (one pixel wide) to conservatively exclude pixels for which the correction for the throughput of the spectrograph optics (contained in the SFLAT reference files) is unreliable. We also implemented the outlier rejection of D’Eugenio et al. (2023). The combination of the eight dithers (with drizzle weighting) allowed us to sub-sample the detector pixels, resulting in cube spaxels with a size of $0.05''$ (corresponding to ~ 20 pc per spaxel).

The resulting data cubes are known to show sinusoidal modulations in single spaxel spectra, caused by the undersampling of the point-spread function (PSF). To correct these so-called “wiggles”, we applied the methodology presented in Perna et al. (2023), and adapted to the Arp 220 dataset as reported in Ulivi et al. in prep.. However, we note that these wiggles do not affect the results presented in this work, because we use spatially integrated spectra, which are much less affected by PSF undersampling (e.g. Law et al. 2023).

In addition to the Arp 220 dataset, in this manuscript we present the JWST/NIRSpec observations of another extragalactic source, the nearby LIRG VV114 (programme 1328, PI: L. Armus; e.g. Rich et al. 2023). They were reduced following the same procedure reported above.

Therefore, for both Arp 220 and VV114 we obtained three data cubes, corresponding to the grating settings G140H/F100LP (referred to as band1 hereinafter), G235H/F170LP (band2), and G395H/F290LP (band3), covering the wavelength range 0.95 – 5.1 μm .

2.2. Astrometric registration

Before analysing the Arp 220 data-cubes, we tested whether they are aligned with each other. We extracted NIRSpec equivalent narrow-band images from the wavelength range 1.85 – 1.87 μm covered by both band1 and band2 cubes; these images are perfectly aligned in the pixel space, although a small discrepancy in the WCS coordinates registration of the reference pixel introduces an offset of $\delta\text{RA} = -0.0047''$ and $\delta\text{DEC} = -0.0141''$. Similarly, we obtained additional narrow-band images covering the range 3.00 – 3.02 μm from the band2 and band3 cubes; also in this case, the images are perfectly aligned in the pixel space, but present a discrepancy in WCS registrations, with $\delta\text{RA} = +0.0017''$ and $\delta\text{DEC} = 0.0071''$. Therefore, we corrected the WCS registrations of the band2 and band3 cubes to match the coordinates in band1.

The absolute astrometric registration is performed using the ALMA 0.1'' resolution maps of continuum emission at 2.6 mm presented by Scoville et al. (2017, project 2015.1.00113.S), and the 0.03'' resolution map of 1.3 mm continuum (project 2017.1.00042.S). We matched the central position of the two nuclei in the NIRSpec narrow-band image, obtained by collapsing the band3 cube in the range 5.1 – 5.12 μm , and in the ALMA images. The narrow wavelength range used to identify the nuclei in the NIR has been preferred to those at shorter wavelengths, as the latter are significantly more affected by dust extinction (see Sect. 3). The astrometry corrections we applied to the three NIRSpec cubes are $\delta\text{RA} = -0.3028''$ and $\delta\text{DEC} = -0.0209''$. This offset is consistent with the expected accuracy of JWST pointing

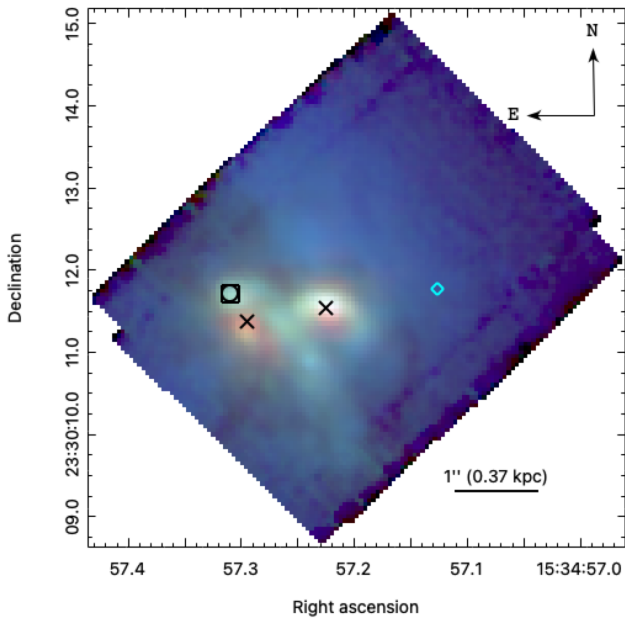


Fig. 1: Three-colour near-infrared image of Arp 220 obtained by combining NIRSpec narrow-band images tracing the continuum emission at $\sim 1 \mu\text{m}$ (blue), $3 \mu\text{m}$ (green) and $5 \mu\text{m}$ (red). The positions of the W and E nuclei are marked with x symbols and match those of the nuclear pc-scale disks observed in the mm with ALMA (Scoville et al. 2017). The box-circle symbol marks the position of a bright cluster. The cyan diamond indicates a region with fast multi-phase outflows.

without a dedicated target acquisition procedure (Böker et al. 2023).

3. Analysis

The two Arp 220 nuclei separated by $\sim 1''$ are visible in the infrared (e.g. Scoville et al. 1998), millimetre (e.g. Scoville et al. 2017; Lamperti et al. 2022), radio (e.g. Baan & Haschick 1995), and X-ray (e.g. Lockhart et al. 2015). Figure 1 shows the composite near-infrared image of Arp 220 obtained from the combination of three NIRSpec narrow-band images extracted from the reduced data-cube at $\sim 1 \mu\text{m}$ (blue), $3 \mu\text{m}$ (green) and $5 \mu\text{m}$ (red), covering a Field of View (FoV) of $5'' \times 4''$. The position of the W and E nuclei are marked for visual purposes.

The Arp 220 nuclear morphology is strongly influenced by dust extinction, even in the NIR (see also Fig. A.1). The continuum emission appears as a crescent arc above the W nucleus at $\sim 1 \mu\text{m}$ and $\sim 3 \mu\text{m}$. The E nucleus is barely visible at these wavelengths, but a few bright, clumpy regions likely associated with clusters can be identified (see also Scoville et al. 1998). Among them, we marked with a box-circle the position of the brightest clump at the north of the E nucleus; hereinafter, we refer to it as the NE cluster, although it may be part of a more extended structure connecting the blue clumps in the regions between the nuclei in Fig. 1. The emission at $\sim 5 \mu\text{m}$ is mostly dominated by the two unresolved nuclei, marked in the figure with two crosses.

3.1. Spectral extraction

We extracted the spectra of the two nuclei and the NE cluster shown in Fig. 1 for each of the three NIRSpec gratings. We used apertures of three spaxels in radius, corresponding to $0.15''$ or

55 pc. This aperture size broadly corresponds to two NIRSpec spatial resolution elements at $5 \mu\text{m}$ (FWHM $\sim 0.15''$; D'Eugenio et al. 2023), thus ensuring that the entire point-source flux is captured at all wavelengths.

The three spectra are reported in Fig. 2; they are shown in rest-frame, taking into account their relative redshifts: $z_W = 0.01774$, $z_E = 0.01839$, and $z_{NE} = 0.01870$ (see Table 1). These values are obtained by measuring the centroid of the brightest hydrogen lines, and are comparable with those inferred from sub-mm/mm ALMA spectroscopy at angular resolutions similar to those of NIRSpec (see Sect. 4.1).

The spectra show a few gaps in wavelength coverage in the middle of the three bands, due to the gap between the two NIRSpec detectors. The overlapping wavelength ranges at $\sim 1.85 \mu\text{m}$ and $\sim 3 \mu\text{m}$ show a perfect match between the different bands, demonstrating a consistent flux calibration. We note that no aperture corrections are taken into account in this work.

3.2. Identification of the lines

The identification of the multitude of emission lines detected in NIRSpec spectra of Arp 220, and marked in Fig. 2 with vertical lines, was performed using compilations of NIR features in star-forming and active galaxies from the literature (e.g. Lutz et al. 2000; Koo et al. 2016; Lamperti et al. 2017; Lee et al. 2017; Riffel et al. 2019). We also use the NIST atomic spectra database¹ (Ralchenko 2005) and the HITRAN (high-resolution transmission molecular absorption database², Rothman 2021) to provide probable identifications of faint lines that, to our knowledge, have not previously been reported in the literature.

Figures B.1-B.6 report all species identified in the spectra of the Arp 220 nuclei and the NE cluster, in comparison with those in the nuclear regions of another nearby interacting LIRG observed with NIRSpec, VV114 (e.g. Rich et al. 2023). Firmly detected line transitions are indicated with solid vertical lines, and are also reported in Table 2. Probable identifications are marked in the figures in the Appendix with dotted vertical lines. All emission lines are well visible in the spectra of the south-west nucleus of VV114 (named SWc2 by González-Alfonso et al. 2023), at higher signal-to-noise and with narrower profiles than in Arp 220. All three nuclear regions of VV114, namely NE, SW, and SWc2, have been suggested to harbor deeply obscured AGN (e.g. Rich et al. 2023; González-Alfonso et al. 2023). Hence, they serve as an optimal benchmark for comparison with the nuclei of Arp 220, which are also presumed to contain obscured AGN.

3.3. Modelling of the continuum emission

To fit the stellar continuum, we used the penalised-pixel-fitting routine pPXF (Cappellari 2017). We used the MARCS synthetic library of stellar spectra to model the stellar continuum (Gustafsson et al. 2008); these templates have a constant spectral resolution $\Delta\lambda/\lambda = 20000$ ($\sigma \sim 6 \text{ km s}^{-1}$) and cover the range $0.13 - 20 \mu\text{m}$ with wavelengths in vacuum. Although not as reliable as an empirical stellar library, MARCS templates were preferred to E-MILES (Vazdekis et al. 2016), which have lower spectral resolution than our NIRSpec data, and XSL (Verro et al. 2022), which have narrower wavelength coverage and are affected by telluric features.

¹ <https://www.nist.gov/pml/atomic-spectra-database>

² <https://hitran.org/>

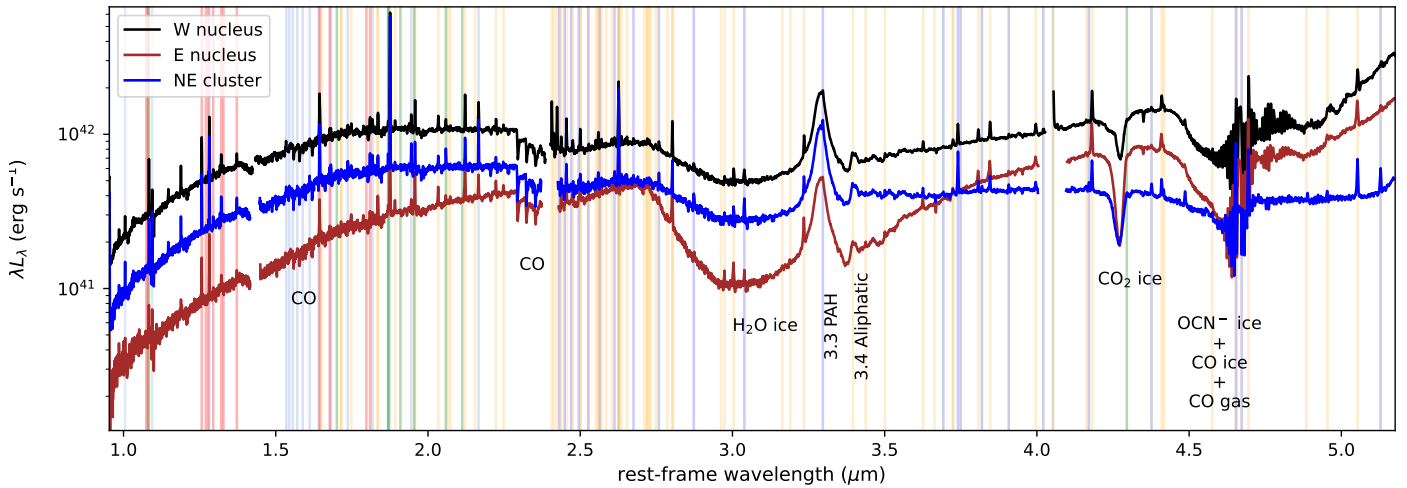


Fig. 2: Arp 220 NE cluster, W and E nuclear spectra from the three NIRSpc gratings. The spectra are shown in luminosity as a function of the rest frame wavelength. Vertical blue lines mark the positions of hydrogen transitions (dark to light blue colours indicate distinct hydrogen series); orange lines identify H_2 lines; red lines are associated with $[\text{Fe II}]$ transitions; green lines mark He I emission features. Strong broad-band absorption and emission features are also labelled in the figure.

Table 1: Properties of Arp220 nuclear regions

	W nucleus	E nucleus	NE cluster
RA (J2000)	15:34:57.224	15:34:57.294	15:34:57.309
DEC (J2000)	+23:30:11.515	+23:30:11.353	+23:30:11.698
redshift (H I)	0.01774 ± 0.00001	0.018396 ± 0.00001	0.018704 ± 0.00001
redshift (stars)	0.0179 ± 0.0003	0.0183 ± 0.0002	0.0186 ± 0.0001
SFR(radio/far-IR) [$M_\odot \text{ yr}^{-1}$]	110 – 150	60 – 80	–
SFR($\text{Pa}\alpha_{\text{corr}}$) [$M_\odot \text{ yr}^{-1}$]	$0.52^{+0.16}_{-0.06}$	0.17 ± 0.02	0.94 ± 0.02
SFR(PAH 3.3 μm) [$M_\odot \text{ yr}^{-1}$]	3.4 ± 0.2	1.5 ± 0.2	1.9 ± 0.2
A_V [mag]	$10.6^{+1.7}_{-0.5}$	$14.1^{+0.6}_{-0.3}$	11.2 ± 0.1
$\log(n_e/[\text{cm}^{-3}])$	3.7 ± 0.1	4.5 ± 0.4	3.6 ± 0.1

Notes: SFR measurements are corrected for dust extinction using the A_V reported in the table; the latter are obtained from Eq. 1, assuming $R_V = 3.1$. Radio and far-IR based SFR measurements come from Varenus et al. (2016) and Pereira-Santaella et al. (2021), respectively.

We also adopted a sixth-order multiplicative polynomial to better reproduce the spectral continuum shape. In addition, we used a set of gas emission line templates (parametrised with Gaussian profiles) together with the stellar ones to guide the fit. We conducted separate fits for the band1 (0.95 – 1.86 μm) and band2 (1.63 – 3.11 μm) cubes, with the latter restricted to wavelengths below 2.4 μm , corresponding to the cutoff of the detector gap. For band1, the wavelengths falling within the NIRSpc detector gap were appropriately masked during the fit procedure.

Since no prominent stellar features are observed at wavelengths above 2.4 μm , and because of the presence of dust emission and ice absorption (e.g. Donnan et al. 2024), we preferred to model the pseudo-continuum with a Savitzky–Golay filter after masking all prominent emission and absorption features.

In Figs. B.1-B.3 we report the reconstructed pPXF best-fit continuum emission, while Figs. B.4-B.6 show the pseudo-continuum shape in the two Arp220 nuclei and the NE cluster. We used the (pseudo)-continuum-subtracted spectra to model the emission lines, and hence derive the ISM kinematic and physical properties in these three regions.

3.4. Modelling of the emission lines

After subtracting the (pseudo)-continuum, we modelled the most relevant gas emission lines using a combination of Gaussian profiles. In particular, we modelled a set of H I recombination lines - Paschen (Pa), Brackett (Br), Pfund (Pf), and Humphreys (Hu) series - and molecular hydrogen features, as well as singly ionised iron transitions.

The sets of H I, H_2 and $[\text{Fe II}]$ transitions are modelled using independent fits, to account for the fact that these three species can trace different gas phases and can have therefore different systemic velocities and line widths (e.g. May & Steiner 2017). All transitions were fitted using the Levenberg–Markwardt least-squares fitting code CAP-MPFIT (Cappellari 2017).

The transitions of a given species were fitted simultaneously (e.g. Perna et al. 2015), as it allows to better constrain the properties of the transitions associated with lower S/N. Namely, we constrained the wavelength separation between emission lines in accordance with atomic physics (considering their vacuum wavelengths); moreover, we fixed their widths (in km s^{-1}) to be the same for all the emission lines. Some emission lines are covered by two cubes (e.g. $\text{Br}\epsilon$ at $\sim 1.82 \mu\text{m}$, in band1 and band2 spectra); for these lines we obtained an average profile by considering the errors from individual cubes as weights.

Table 2: Arp 220 emission line list in the W and E nuclei, and NE cluster (band1 spectra)

line	λ_{vac} (μm)	f_W ($10^{-18} \text{ erg s}^{-1} \text{ cm}^{-2}$)	f_E ($10^{-18} \text{ erg s}^{-1} \text{ cm}^{-2}$)	f_{NE} ($10^{-18} \text{ erg s}^{-1} \text{ cm}^{-2}$)
[S III]	0.953321	$598.0^{+0.4}_{-0.4}$	$54.9^{+1.1}_{-1.2}$	$438.0^{+1.8}_{-1.0}$
Pa ϵ	0.954865	$87.9^{+1.5}_{-1.0}$	$7.8^{+1.0}_{-0.8}$	$41.7^{+1.9}_{-0.8}$
[C I]	0.982412	$11.3^{+1.2}_{-1.1}$	$3.3^{+1.8}_{-0.6}$	$8.8^{+1.8}_{-0.9}$
[C I]	0.985295	$63.7^{+1.2}_{-0.5}$	$15.5^{+1.4}_{-0.9}$	$28.8^{+0.0}_{-0.3}$
Pa δ	1.005219	$112.0^{+1.4}_{-1.5}$	$15.8^{+1.2}_{-1.0}$	$67.6^{+1.6}_{-0.8}$
[S II]	1.028955	$48.3^{+5.2}_{-2.7}$	$5.7^{+4.2}_{-1.5}$	$11.6^{+2.5}_{-1.6}$
[S II]	1.032332	$62.6^{+2.5}_{-2.2}$	$0.9^{+0.0}_{-0.0}$	$13.6^{+2.7}_{-1.6}$
[S II]	1.033924	$63.1^{+2.6}_{-2.2}$	$5.3^{+2.4}_{-1.9}$	$17.2^{+2.6}_{-1.4}$
[S II]	1.037334	$39.3^{+0.1}_{-0.3}$	$0.9^{+1.4}_{-0.9}$	$11.1^{+2.7}_{-2.7}$
[N I]	1.040059	$42.8^{+0.1}_{-0.0}$	$4.2^{+2.9}_{-3.2}$	$3.8^{+2.5}_{-2.8}$
He I	1.083331	$628.0^{+2.2}_{-1.1}$	$41.2^{+1.3}_{-0.4}$	$185.0^{+1.0}_{-0.7}$
Pa γ	1.094116	$167.0^{+1.7}_{-1.6}$	$25.5^{+1.1}_{-0.6}$	$205.0^{+1.7}_{-1.9}$
[P II]	1.147134	$101.0^{+1.4}_{-0.9}$	$9.4^{+1.0}_{-0.5}$	$45.7^{+1.2}_{-0.7}$
[P II]	1.188605	$328.0^{+1.3}_{-0.7}$	$27.8^{+0.7}_{-0.3}$	$126.0^{+0.9}_{-0.8}$
[Ni II]	1.191000	$31.5^{+1.3}_{-0.6}$	$5.0^{+0.6}_{-0.7}$	$19.6^{+1.1}_{-0.8}$
[Fe II]	1.257021	$711.0^{+10.6}_{-4.3}$	$78.0^{+3.6}_{-1.8}$	$371.0^{+7.2}_{-3.8}$
[Fe II]	1.270690	$44.5^{+5.1}_{-2.2}$	$0.8^{+1.7}_{-0.0}$	$10.8^{+6.6}_{-3.6}$
[Fe II]	1.278789	$75.6^{+3.7}_{-1.6}$	$3.3^{+6.0}_{-2.5}$	$26.7^{+5.5}_{-3.1}$
Pa β	1.282167	$1170.0^{+6.7}_{-7.0}$	$124.0^{+4.6}_{-2.6}$	$822.0^{+6.5}_{-4.1}$
[Fe II]	1.294453	$71.7^{+6.6}_{-2.5}$	$7.1^{+2.8}_{-2.0}$	$24.6^{+5.3}_{-2.0}$
[Fe II]	1.320911	$289.0^{+7.0}_{-4.5}$	$26.9^{+3.2}_{-2.0}$	$130.0^{+4.6}_{-3.8}$
[O I]	1.316871	$94.2^{+5.3}_{-2.5}$	$4.0^{+3.0}_{-2.4}$	$22.6^{+5.3}_{-2.2}$
[Fe II]	1.372200	$185.0^{+6.1}_{-4.3}$	$25.0^{+2.9}_{-1.2}$	$102.0^{+4.3}_{-2.0}$
Br 13	1.611378	$51.6^{+6.9}_{-3.6}$	$9.2^{+3.5}_{-3.0}$	$54.0^{+5.2}_{-3.8}$
Br 12	1.641174	$71.3^{+6.6}_{-4.2}$	$11.0^{+2.9}_{-4.5}$	$7.6^{+4.0}_{-3.8}$
[Fe II]	1.644002	$1340.0^{+11.1}_{-5.7}$	$209.0^{+8.5}_{-3.9}$	$787.0^{+9.6}_{-8.6}$
[Fe II]	1.677300	$160.0^{+6.6}_{-5.2}$	$20.3^{+6.4}_{-2.7}$	$67.3^{+5.8}_{-5.1}$
Br 11	1.681118	$166.0^{+7.2}_{-7.0}$	$27.7^{+5.1}_{-2.5}$	$117.0^{+5.5}_{-3.3}$
H ₂	1.714881	$14.9^{+72.8}_{-11.3}$	$2.6^{+40.5}_{-0.1}$	$2.5^{+0.0}_{-0.0}$
H ₂	1.714958	$88.8^{+4.6}_{-59.5}$	$30.3^{+12.3}_{-20.1}$	$29.4^{+5.0}_{-7.0}$
H ₂	1.748101	$176.0^{+5.6}_{-8.6}$	$43.8^{+18.9}_{-8.3}$	$66.1^{+1.2}_{-5.9}$
Br 10	1.736692	$202.0^{+6.3}_{-6.4}$	$17.4^{+4.5}_{-2.5}$	$111.0^{+6.9}_{-7.2}$
Br ϵ	1.817916	$245.0^{+11.5}_{-5.7}$	$34.0^{+8.3}_{-4.5}$	$168.0^{+12.7}_{-4.5}$
H ₂	1.834123	$23.1^{+11.9}_{-4.2}$	$57.8^{+12.6}_{-22.0}$	$37.6^{+8.2}_{-7.0}$
H ₂	1.835913	$370.0^{+12.4}_{-6.9}$	$109.0^{+39.8}_{-13.4}$	$145.0^{+10.8}_{-3.7}$

Notes: This list comprises all emission lines detected in band1; see Tables C.1 and C.2 for the ones in band2 and band3, respectively. The reported fluxes are obtained within apertures of 0.3'' in diameter from single Gaussian fits, without dust- and aperture-corrections.

For each species we performed two fits, with one and two Gaussian components per emission line respectively. The number of Gaussian sets (i.e. distinct kinematic components) used to model the lines of a specific species was determined on the basis of the Bayesian information criterion (BIC; Schwarz 1978).

The measured fluxes of all identified emission line transitions are reported in Tables 2, C.1 and C.2. To streamline the presentation, all tabulated fluxes are derived from single Gaussian fits; detailed Gaussian decomposition of bright line profiles is discussed in Sect. 4.

4. Results

In this section, we report the general characterisation of the nuclei and the NE cluster, in terms of spectral shape, extinction, electron density, and presence of outflows. These properties are

discussed in Sect. 5 to investigate the possible presence of AGN signatures.

4.1. Systemic redshift of the two nuclei

The comparison of the three selected regions in Arp 220 was performed after reporting the individual spectra in luminosity (λL_λ) as a function of the rest-frame wavelength in vacuum. We used the centroid of the H I lines to determine the redshifts for the three spectra. In fact, these lines are quite symmetric and narrow and, therefore, are likely less affected by outflows and perturbed motions than other lines (see Perna et al. 2020; Wheeler et al. 2020). In contrast, the brightest H₂ and [Fe II] lines show prominent blue wings and are blue-shifted by a few 10s km s⁻¹ with respect to the H I lines (Table 3).

The redshifts inferred from the atomic hydrogen lines are reported in Table 1. These values are consistent with those obtained from the stellar continuum modelling, within the uncertainties (see Table 1). Moreover, our measurements match the ones obtained from the study of sub-mm/mm molecular line transitions as reported in Sakamoto et al. (2021b), $z_W \sim 0.01768$ and $z_E \sim 0.01808$, and Pereira-Santaella et al. (2021), $z_W \sim 0.01765$ and $z_W \sim 0.01797$. In particular, for the W nucleus, all measurements are consistent within $\sim 20 \text{ km s}^{-1}$. The molecular lines in the E nucleus are quite asymmetric (see Fig. 1 in Sakamoto et al. 2021b), resulting in slightly larger discrepancies compared to our NIR redshift. However, all measurements remain consistent within $\lesssim 100 \text{ km s}^{-1}$, suggesting minimal relative motions between the various components.

4.2. Qualitative comparison between Arp 220 nuclear regions and the bright cluster

The spectra of the two nuclei and the NE cluster contain a high number of emission lines: among them hydrogen lines (from the Pa, Br, Pf, and Hu series), as well as helium, iron, and molecular hydrogen transitions. Notably, H I lines appear a few times fainter in the E spectrum compared to the W and NE spectra, likely due to higher extinction levels (see Sect. 4.3) and lower SFR (Sect. 5.1). The W nucleus displays the most intense H₂ lines, approximately $2\times$ stronger than those in the E and NE spectra.

At $3.3 \mu\text{m}$, all three spectra show a broad emission feature produced by polycyclic aromatic hydrocarbons (PAHs); the $3.4 \mu\text{m}$ aliphatic features are also present in all three locations. PAHs and aliphatic transitions are stronger in the W nucleus, by a factor of ~ 3 (2) with respect to the E nucleus (NE cluster; see Sect. 5.1). This suggests that the SFR is higher in the W nucleus (as PAHs trace recent star formation activity; Sect. 5.1).

The prominent CO absorption bands at $\sim 1.6 \mu\text{m}$ and between $2.3 \mu\text{m}$ and $2.4 \mu\text{m}$, produced in the atmospheres of giant and supergiant stars (Oliva et al. 1995) are clearly visible in the two nuclei as well as in the NE cluster.

Various other broad-band absorption features are visible as well, mostly produced by solid state molecules of water-ice (H₂O, at 3 and $4.5 \mu\text{m}$), and carbon monoxide (CO, at $4.67 \mu\text{m}$) transitions. These absorption features are stronger in the nuclear regions than in the nearby cluster; the $3.3 - 3.8 \mu\text{m}$ “ice band wing” (Gibb et al. 2004) is observed only in the two nuclei. The strength of these absorption bands is therefore likely correlated with the abundance of dust, given that the two nuclear regions are the most obscured in the mm range (Sakamoto et al. 2021a). Conversely, the carbon dioxide ice transitions ¹²CO₂ at $4.27 \mu\text{m}$ and ¹³CO₂ at $4.38 \mu\text{m}$ have rather peculiar shapes in the three spectra: the former is stronger in the E nucleus, but more asymmetric in the W nucleus (with a prominent blue shoulder), while the NE cluster shows intermediate strength with respect to the nuclei. The ¹³CO₂ is deeper and narrower in the W nucleus.

The W and E nuclei of Arp 220 show ¹²CO ro-vibrational lines up to $J_{low} = 23$ (Fig. B.6), indicating the presence of high excitation gas. Such transitions could provide a further indirect evidence of AGN activity. Detailed modelling is required to infer the CO gas properties, and hence test the more likely mechanisms responsible for such high excitation (e.g. Baba et al. 2022; González-Alfonso et al. 2023; Buiten et al. 2023; García-Bernete et al. 2024; Pereira-Santaella et al. 2024). This analysis will be presented in a forthcoming paper (Buiten, van der Werf et al., in prep.).

Differences in the three spectra can also be appreciated from a qualitative comparison between their continuum shapes. Going from the shortest wavelengths to $\sim 1.8 \mu\text{m}$, all three sources show a pronounced steepening in their spectra, likely dominated by the diminishing effect of dust obscuration with increasing wavelength (see also Engel et al. 2011). In the range $1.8 - 2.3 \mu\text{m}$ the W and NE spectra flatten, while the E spectrum still shows the same steepening observed at shortest wavelengths; this could suggest an higher extinction at the position of the E nucleus, due to the dust lane visible in reddish colours in Fig. 1. Between 2.3 and $5 \mu\text{m}$, the nuclear regions show a mild increase in luminosity while NE is almost constant. At $\sim 5 \mu\text{m}$, the spectrum of the NE cluster reveals a modest rise in luminosity, while the two nuclei exhibit a much more pronounced increase likely due to the presence of warm dust (Armus et al. 2007). It is possible therefore that dust-absorbed light is re-emitted at wavelengths $\gtrsim 2 \mu\text{m}$ in the two nuclei; the higher dilution of CO bands at $\sim 2.3 - 2.4 \mu\text{m}$ in the nuclei compared to the NE cluster (Fig. B.3) also supports this possibility, as suggested by Engel et al. 2011.

In the next sections, we will briefly discuss the general properties of some of these components. We do not pursue the full spectral energy distribution modelling further in this work, but instead will use a subsequent paper to focus on a more detailed investigation.

4.3. Extinction

Extinction can have an important effect on the estimated source luminosity and SFR, and we therefore consider different methods for deriving its value. We compared pairs of emission lines at wide wavelength separation, for which the intrinsic ratio of line strengths is known. We calculated the colour excess in terms of Pa β and Br γ ,

$$\begin{aligned} E(B - V) &= \frac{2.5}{k(\text{Pa}\beta) - k(\text{Br}\gamma)} \log_{10} \left(\frac{(\text{Pa}\beta/\text{Br}\gamma)_{\text{obs}}}{(\text{Pa}\beta/\text{Br}\gamma)_{\text{int}}} \right) \\ &= 5.22 \log_{10} \left(\frac{(\text{Pa}\beta/\text{Br}\gamma)_{\text{obs}}}{5.88} \right) \end{aligned} \quad (1)$$

where the intrinsic ratio Pa β /Br γ is set to 5.88 assuming an electron temperature and a density of 10^4 K and 10^3 cm^{-3} respectively (e.g. Osterbrock & Ferland 2006). We also used the Pf γ and Br δ to obtain an independent estimate for the colour excess

$$\begin{aligned} E(B - V) &= \frac{2.5}{k(\text{Br}\delta) - k(\text{Pf}\gamma)} \log_{10} \left(\frac{(\text{Br}\delta/\text{Pf}\gamma)_{\text{obs}}}{(\text{Br}\delta/\text{Pf}\gamma)_{\text{int}}} \right) \\ &= 8.95 \log_{10} \left(\frac{(\text{Br}\delta/\text{Pf}\gamma)_{\text{obs}}}{1.71} \right) \end{aligned} \quad (2)$$

where the intrinsic ratio Br δ /Pf γ is set to 1.71 (with the same assumptions as reported above). The coefficients in Eqs. 1 and 2 were derived assuming a Cardelli et al. (1989) extinction law.

We derived an additional estimate of the colour excess from the flux ratio of [Fe II] at 1.257 and $1.644 \mu\text{m}$ (e.g. Riffel et al. 2014), which are the two strongest iron lines in the NIR regime,

$$E(B - V) = 8.95 \log_{10} \left(\frac{1.34}{([\text{FeII}]_{1.257}/[\text{FeII}]_{1.644})_{\text{obs}}} \right) \quad (3)$$

where 1.34 is the intrinsic ratio (we note, however, that this is still a matter of some debate, and different values are reported in the literature, from 1.04 to 1.49, see Eriksen et al. 2009).

We measured a colour excess of the order of a few magnitudes ($\sim 3 - 5$) in the three regions of interest, corresponding to $A_V \sim 10 - 14$ (assuming $R_V = 3.1$). We do not observe significant differences in the measurements obtained from the three diagnostic ratios above mentioned (Eqs. 1, 2, 3). Therefore, hereinafter we will refer to the results obtained from Eq. 1. The most extreme extinction is associated with the E nucleus, with $A_V \sim 14$, consistent with the presence of the strongest steepening in continuum emission at wavelengths $\lesssim 2 \mu\text{m}$ with respect to the W nucleus and the NE cluster (with $A_V \sim 11$, see Table 1).

In previous studies, an extinction of ≈ 6 mag in the innermost nuclear regions of Arp 220 was reported, employing diagnostics such as the H I flux ratios $\text{H}\alpha/\text{H}\beta$ (Perna et al. 2020), $\text{H}\alpha/\text{Pa}\beta$ (Giménez-Arteaga et al. 2022), and $\text{Pa}\alpha/\text{Br}\gamma$ (Engel et al. 2011). More extreme measurements were obtained from mid-infrared diagnostics: for instance, Haas et al. (2001) reported an extinction of a few tens of magnitudes. This suggests that NIRSpec observations may only probe the outer gaseous layers, and that the total extinction towards the core of these dusty regions can be much higher than $A_V \sim 10 - 14$.

4.4. Electron density

We derived the electron density in the line-emitting regions surrounding the E, W, and NE regions of Arp 220 via the comparison of observed line strength ratios of [Fe II] transitions with theoretical values.

We used the ratio [Fe II] $1.677 \mu\text{m}/1.644 \mu\text{m}$ to infer electron densities in the range $\log n_e \approx 3.5 - 4.5 \text{ cm}^{-3}$ for the three regions of interest (from Eq. 6 in Koo et al. 2016). For the two nuclei, for which two kinematic components are required to fit the total profiles, we consider the narrow components (as the broad one is undetected in the faint [Fe II] $1.677 \mu\text{m}$). These measurements, reported in Table 1, are discussed in the context of previous measurements in Sect. 5.2.

4.5. Nuclear outflows

A distinctive feature of Arp 220's nuclear environment is the presence of powerful and complex outflows. Compact and collimated cold molecular outflows, with velocities of a few 100 km s^{-1} , a bipolar morphology and an extension of $\sim 120 \text{ pc}$, are observed in both nuclei (e.g. Wheeler et al. 2020). Broader line profiles are instead observed in the ionized and atomic gas: for instance, Perna et al. (2021) reported W80 velocities (defined as the difference between the 90th- and 10th-percentile velocities of the fitted line profile) of $\sim 800 \text{ km s}^{-1}$. However, these measurements have been obtained from observations at lower spatial resolution ($\sim 200 \text{ pc}$), and likely cannot be used to properly resolve the outflow kinematics on smaller scales.

Figure 3 shows the integrated spectra in the vicinity of the $\text{Pa}\alpha$ (top), [Fe II] $1.644 \mu\text{m}$ (centre), and H_2 $2.12 \mu\text{m}$ (bottom) lines for the three regions of interest. The NE cluster shows symmetric and narrow profiles; conversely, broad and asymmetric (preferentially blue-shifted) line shapes are observed in both nuclear regions, with outflowing gas at velocities up to -500 km s^{-1} . In this work, we consider as outflow velocity $v_{\text{max}} = \Delta V_{\text{broad}} + 2\sigma_{\text{broad}}$, where σ_{broad} is corrected for instrumental resolution (e.g. Fluetsch et al. 2021). In Table 3 we report the best-fit kinematic parameters, considering both non-parametric (e.g. W80), and parametric outflow velocity measurements (e.g. v_{max} ; see caption of Table 3 for details).

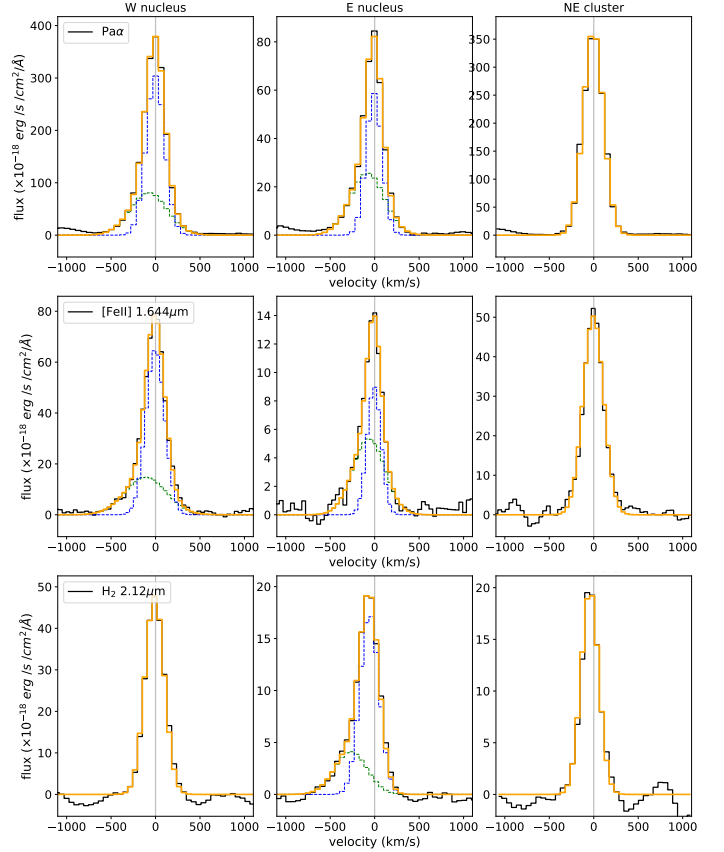


Fig. 3: Continuum-subtracted integrated spectra of the three regions of interest in the vicinity of the $\text{Pa}\alpha$, [Fe II] $1.644 \mu\text{m}$, and H_2 $2.12 \mu\text{m}$. The original spectra (in black) are reported in velocity space. The best-fit emission line profiles are shown in orange; the individual Gaussian profiles used to reproduce the line shapes are reported in blue and green. Broad and asymmetric profiles are found in the nuclear spectra. The vertical lines mark the zero-velocity as inferred from the narrow component of H I lines.

A more detailed discussion about the presence of AGN winds possibly responsible for the broad and asymmetric profiles observed in the Arp 220 nuclei is presented in Sect. 5.3.

5. Discussion

We used the aperture-extracted spectra of the obscured nuclei E and W and the bright cluster NE to identify all gas emission line features in the NIRSpec spectral range, as well as the main absorption features due to dust and stars. We identified ~ 70 ionized gas and ~ 50 molecular emission lines; Tables 2, C.1, and C.2 give the (vacuum) wavelengths and fluxes for all the firmly identified features in Arp220, while Table 3 displays the kinematic parameters of the main optical lines discussed in this paper. We note that a few well detected emission lines are not tabulated, as (i) their modelling would require detailed deblending from other lines, or (ii) their observed wavelengths are very close to the edges of the NIRSpec detector gaps.

In this section we discuss the main spectral features observed in the spectra reported in Fig. 2 in relation with the possible presence of intense episodes of starburst activity and AGN accretion in the two nuclei.

Table 3: Kinematic parameters

W nucleus				
	H I	H ₂	[Fe II]	[Mg IV]
ΔV_1	0 ± 1	-1^{+26}_{-4}	0^{+2}_{-1}	-111 ± 3
FWHM ₁	238 ± 2	250^{+24}_{-6}	242^{+6}_{-4}	234^{+6}_{-10}
ΔV_2	-72 ± 2	–	-110^{+16}_{-8}	–
FWHM ₂	480^{+6}_{-4}	–	525^{+24}_{-9}	–
W80	370 ± 3	270 ± 20	380 ± 3	260 ± 10
V10	-250 ± 2	-180 ± 15	-270 ± 6	-265 ± 10
V_{max}	-480^{+9}_{-4}	-220^{+30}_{-3}	-560 ± 25	-309 ± 8
E nucleus				
	H I	H ₂	[Fe II]	[Mg IV]
ΔV_1	0^{+10}_{-2}	-40 ± 5	-8^{+8}_{-3}	-130^{+14}_{-8}
FWHM ₁	205^{+9}_{-27}	230 ± 3	180^{+45}_{-70}	370^{+20}_{-14}
ΔV_2	-70^{+60}_{-10}	-201^{+13}_{-7}	-60 ± 30	–
FWHM ₂	425^{+50}_{-60}	405 ± 10	420^{+120}_{-60}	–
W80	370 ± 30	440 ± 50	380 ± 42	400 ± 30
V10	-250 ± 20	-370 ± 30	-250 ± 42	-370 ± 20
V_{max}	-430^{+70}_{-45}	-540^{+20}_{-10}	-430^{+140}_{-90}	-440 ± 20
NE cluster				
	H I	H ₂	[Fe II]	[Mg IV]
ΔV_1	0^{+4}_{-3}	-40 ± 5	-14^{+7}_{-8}	-81^{+6}_{-3}
FWHM ₁	260^{+30}_{-3}	225^{+10}_{-60}	210 ± 30	260 ± 10
ΔV_2	–	–	11^{+33}_{-6}	–
FWHM ₂	–	–	340^{+170}_{-40}	–
W80	250 ± 10	270^{+10}_{-50}	290 ± 40	305 ± 40
V10	-160 ± 10	-180^{+10}_{-30}	-170 ± 30	-240 ± 30
V_{max}	-230^{+25}_{-3}	-230^{+10}_{-60}	-190 ± 20	-300 ± 6
NW outflow				
	H I	H ₂	[Fe II]	[Mg IV]
ΔV_1	-175^{+30}_{-10}	-180^{+16}_{-7}	-290^{+15}_{-10}	–
FWHM ₁	130^{+80}_{-20}	80^{+20}_{-45}	640^{+50}_{-30}	–
ΔV_2	-340^{+40}_{-30}	-260^{+70}_{-30}	–	–
FWHM ₂	650^{+105}_{-50}	650^{+60}_{-70}	–	–
ΔV_3	–	85^{+11}_{-6}	–	–
FWHM ₃	–	210^{+50}_{-30}	–	–
W80	680^{+90}_{-30}	715 ± 10	715 ± 40	–
v10	-690 ± 30	-590 ± 15	-670 ± 35	–
v_{max}	-890^{+130}_{-45}	-820 ± 35	-810^{+120}_{-45}	–

Notes: all kinematic parameters are given in km s⁻¹. Velocity shifts ΔV_i and line widths FWHM_{*i*} refer to the individual Gaussian components (*i* = 1 to 3, at maximum) required to model the emission line profiles. V10 is defined as 10th-percentile velocity of the fitted line profile, while W80 is defined as the difference between the 90th- and 10th-percentiles. v_{max} is defined as $\Delta V_{broad} + 2\sigma_{broad}$.

5.1. Star-formation tracers

We derived the instantaneous (~ 10 Myr) SFR from the Pa α dust corrected luminosity, following [Giménez-Arteaga et al. \(2022\)](#), and assuming a [Chabrier 2003](#) initial mass function):

$$\begin{aligned}
 SFR [M_{\odot} \text{ yr}^{-1}] &= 4.4 \times 10^{-42} \times \left(\frac{H\alpha}{Pa\alpha} \right)_{int} \times L(Pa\alpha)_{corr} [\text{erg s}^{-1}] \\
 &= 3.7 \times 10^{-41} \times L(Pa\alpha)_{corr} [\text{erg s}^{-1}]
 \end{aligned}
 \tag{4}$$

where the dust-corrected Pa α luminosity can be obtained with $A(Pa\alpha) = k(Pa\alpha) \times E(B-V)$. In deriving Eq. 4 we assumed electron density of 10^3 cm^{-3} (the dependence from n_e is very weak) and temperature of 10^4 K . Moreover, for the E and W nuclear emission we consider only the narrow components (dashed blue Gaussian lines in Fig. 3), thus excluding the contribution of outflowing material.

The use of E(B-V) inferred from Pa β /Br γ imply dust corrections of $\sim 5 - 8\times$ factors for the Pa α flux, resulting in a SFR $\sim 0.5 M_{\odot} \text{ yr}^{-1}$ for the W nucleus, $\sim 0.2 M_{\odot} \text{ yr}^{-1}$ for the E nucleus, and $\sim 0.9 M_{\odot} \text{ yr}^{-1}$ for the NE cluster. Therefore, these three regions account for a total SFR(Pa α) $\sim 2 M_{\odot} \text{ yr}^{-1}$. Considering the extraction regions of $\sim 0.01 \text{ kpc}^2$, these values would be translated in star-formation surface densities $\Sigma_{SFR} \sim 20 - 100 M_{\odot} \text{ yr}^{-1} \text{ kpc}^{-2}$.

We also use the calibration of SFR for the $3.3 \mu\text{m}$ PAH from [Kim et al. \(2012\)](#), see their Eq. 5) to convert the measured luminosities ($L(\text{PAH}) \sim 2 \times 10^{40} \text{ erg s}^{-1}$ for the W, $L(\text{PAH}) 7 \times 10^{39} \text{ erg s}^{-1}$ for the E, and $L(\text{PAH}) 10^{40} \text{ erg s}^{-1}$ for NE) in L(IR), and then the [Kennicutt & Evans \(2012\)](#)³ relation to derive dust-corrected SFR(PAH) in the range $\sim 1.5 - 3.4 M_{\odot} \text{ yr}^{-1}$ (see Table 1).

In previous optical and NIR studies of Arp 220, slightly higher SFR measurements were obtained when integrating over the whole galaxy: [Perna et al. \(2020\)](#) reported SFR($H\alpha$) $\lesssim 10 M_{\odot} \text{ yr}^{-1}$ (using the Balmer decrement to correct for extinction), while [Giménez-Arteaga et al. \(2022\)](#) obtained SFR(Pa β) $\sim 19 M_{\odot} \text{ yr}^{-1}$ from HST narrow-band images (using Pa β / $H\alpha$ for the dust-correction). [Giménez-Arteaga et al. \(2022\)](#) also reported the total SFR inferred from the $24 \mu\text{m}$ luminosity, $76 M_{\odot} \text{ yr}^{-1}$; this value is significantly less affected by dust ($A_V \sim 90$ would imply a correction of a factor 2 at $24 \mu\text{m}$). This value is more consistent with the total SFR(PAH) $\sim 40 M_{\odot} \text{ yr}^{-1}$ we measure from NIRSpect data using an integrated spectrum extracted over a very large aperture ($r = 1.5''$, i.e. 0.56 kpc).

Therefore, our NIRSpect-based outcomes are definitely in line with previous estimates obtained from optical, NIR, and mid-infrared bands. However, it is worth noting that the SFR inferred from the radio and sub-mm/mm regime appears to be several times higher, reaching $200\text{--}250 M_{\odot} \text{ yr}^{-1}$ (e.g. [Varenius et al. 2016](#); [Pereira-Santaella et al. 2021](#)). In particular, these authors reported SFR $\sim 60\text{--}80 M_{\odot} \text{ yr}^{-1}$ and $\sim 110\text{--}150 M_{\odot} \text{ yr}^{-1}$ for the E and W nuclei separately, hence significantly higher than our NIR-based nuclear measurements. This discrepancy may stem from a combination of factors: (i) The far-IR and radio emission might not be solely attributable to star formation, but could also include contributions from AGN, which are totally extinguished in the NIR. (ii) The SFR derived from FIR measurements traces the star formation history over a longer period (up to 100 Myr) compared to the Pa α and PAH features ($\lesssim 10 \text{ Myr}$).

Summarising, the NIRSpect-based SFR measurements do not offer a solution to the existing discrepancy among various star-formation tracers identified in previous studies.

³ Slightly smaller (but consistent) values would be obtained using the [Piqueras López et al. 2016](#) relation.

5.2. High electron densities

The [Fe II]-based electron densities at the position of the two nuclei and the NE cluster ($\log(n_e/\text{cm}^{-3}) \sim 3.7 - 4.5$) consistently exceed those inferred from optical [S II] 6718, 32 Å lines, which are of the order of 200 cm^{-3} (Perna et al. 2020). This suggests that [Fe II] lines, having critical densities higher than [S II] ($n_{\text{crit}} \sim 1600 \text{ cm}^{-3}$ for [S II] 6716 Å; $n_{\text{crit}} \sim 10^4 \text{ cm}^{-3}$ for iron lines), trace post-shock regions with higher compression. An alternative explanation might be that the higher spatial resolution of NIRSpec data ($\sim 0.1''$ at the wavelengths of the n_e -sensitive [Fe II] lines) compared to the MUSE observations ($\sim 0.6''$) enables a better isolation of regions with higher degree of ionisation.

At higher redshift (up to $z \sim 9$), [S II] and [O II] 3727, 30 Å line ratios are systematically used to measure the ISM electron densities; values in the range $\sim 300 - 1000 \text{ cm}^{-3}$ are generally reported for both AGN (e.g. Perna et al. 2017; Cresci et al. 2023) and star-forming galaxies (e.g. Förster Schreiber et al. 2019; Davies et al. 2021; Rodríguez Del Pino et al. 2023; Isobe et al. 2023). Significant correlations between Σ_{SFR} and n_e have been reported in the literature (e.g. Shimakawa et al. 2015), although they cover relatively narrow ranges in both Σ_{SFR} ($\sim 0.1 - 1 \text{ M}_\odot \text{ yr}^{-1} \text{ kpc}^{-2}$) and n_e ($\sim 10 - 10^3 \text{ cm}^{-3}$). From the extrapolation of these relations (e.g. Eq. 3 in Reddy et al. 2023) to the very high Σ_{SFR} measured in Arp 220 (see Sect. 5.1), we would expect $\log(n_e/\text{cm}^{-3}) \sim 3$. However, this value stands roughly 30 times lower than the one measured at the position of the Arp 220 W nucleus using [Fe II] lines. Instead, our measurements more closely resemble electron densities observed in supernova remnants (e.g., Lee et al. 2017) and at the bases of protostar jets (e.g., Davis et al. 2011), with [Fe II]-based densities spanning $\log(n_e/\text{cm}^{-3}) \approx 3.5 - 4.5$.

Therefore, on the basis of available information, we cannot discriminate between the two above mentioned scenarios: the extremely high electron densities we measured in the nuclei and the NE cluster could be due to higher levels of compression and/or ionisation with respect to [S II] gas emitting in the optical. We can definitely exclude any potential contamination from high-density AGN Broad Line Region (BLR) in the [Fe II]-based electron densities obtained for the Arp 220 nuclei, as the forbidden [Fe II] line transitions cannot originate from BLR high-density regions ($N_e(\text{BLR}) \gg N_e([\text{Fe II}])$).

5.3. Presence of multi-phase outflows

The NIRSpec nuclear spectra of Arp220 show ionised and molecular gas transitions with broad profiles and prominent blue wings associated with outflows. In particular, high-velocity components are detected in Pa α and [Fe II] $1.644 \mu\text{m}$ at the position of the E and W nuclei. Prominent H₂ blue wings are solely observed in the E nucleus. This suggests that the high-velocity gas in the W nucleus is sufficiently hot (because of shocks, or intense ultraviolet radiation by hot stars or AGN) to disassociate the H₂ molecules.

The nuclear material can reach velocities of up to $v_{\text{max}} \sim 550 \text{ km s}^{-1}$ (Fig. 3). We anticipate here that such outflows reach distances of $\sim 1 \text{ kpc}$ and velocities of -900 km s^{-1} in the off-nuclear regions covered by NIRSpec (Ulivi et al., in prep.). Figure 4 shows the Pa α and H₂ $2.12 \mu\text{m}$ line profiles extracted from a circular aperture of $r = 0.15''$ at a distance of $\sim 1.3''$ to the west from the W nucleus, as defined in Fig. 1 (cyan diamond); at this position, both ionised and molecular gas have outflow velocities up to 900 km s^{-1} (Table 3). Similar velocities have also been ob-

served in the ionised and atomic gas phases at kpc-scales in the optical regime (e.g. Perna et al. 2020).

Nuclear outflows in NIR H₁, H₂ and iron lines have been observed in nearby ULIRGs and active galaxies. While sources lacking an active SMBH typically exhibit less extreme outflow velocities (on the order of a few hundred km s^{-1}), AGN can manifest outflows across a broad velocity range, from a few hundred to over a thousand km s^{-1} (e.g. Emonts et al. 2017; Perna et al. 2021; Speranza et al. 2022; Villar Martín et al. 2023). Consequently, distinguishing between starburst- and AGN-driven outflows in Arp 220, based solely on velocity estimates, proves to be a challenging task. A more comprehensive analysis of the multi-phase and multi-scale outflows will be necessary to elucidate whether the outflow energetics in Arp 220 are more consistent with AGN or starburst launching mechanisms; this work will be presented in a forthcoming paper, Ulivi et al., in prep..

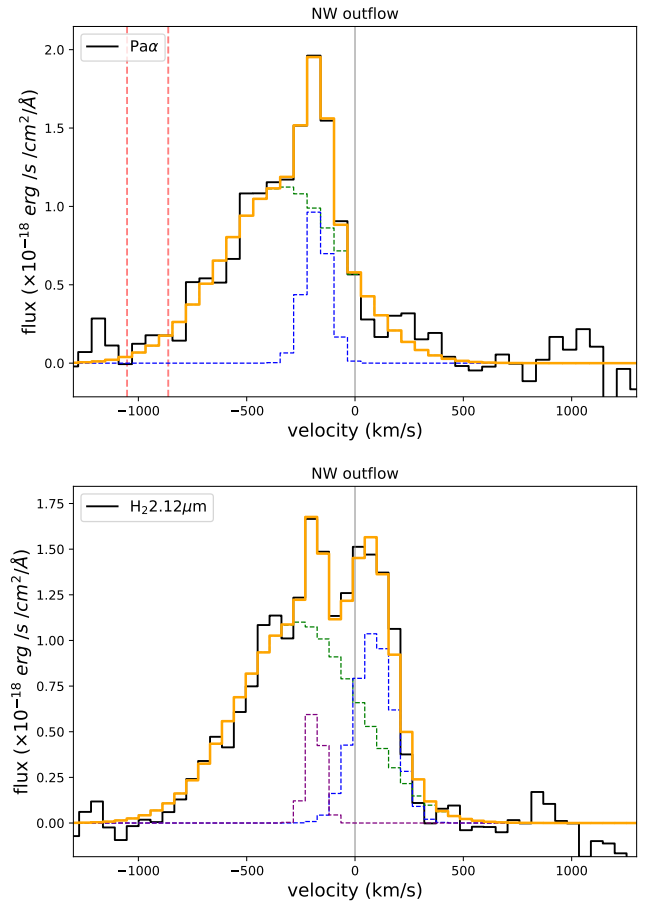


Fig. 4: Observed profiles of Pa α and H₂ $2.12 \mu\text{m}$, showing fast outflows. The spectra are extracted from the region in Fig. 1 marked with a cyan diamond, and reported in velocity space. The best-fit emission line profiles are shown in orange; the individual Gaussian profiles used to reproduce the line shapes are reported in blue, purple, and green. The vertical grey lines mark the zero-velocity of the E nucleus (corresponding to the kinematic centre of Arp 220); the dashed red vertical lines in the top panel identify the He I lines close to Pa α (see Table 2).

5.4. Absence of high-ionisation lines

High excitation emission lines with ionisation potentials $IP > 54$ eV (the He^+ ionisation energy) can be formed either in gas photoionised by hard ultraviolet radiation or in very hot, collisionally ionised plasma. Therefore, they can be used as sign for AGN activity (e.g. Oliva et al. 1994; Moorwood et al. 1997).

Most of these highly ionised lines have previously been identified in ground-based (e.g. Rodríguez-Ardila et al. 2011; Lamperti et al. 2017; Cerqueira-Campos et al. 2021; den Brok et al. 2022) and space-based (e.g. Lutz et al. 2000; Sturm et al. 2002) NIR spectra of some nearby Seyfert galaxies (Table 4). No quantitative studies of the coronal lines prevalence in the AGN population have been made yet; however, there are indications for a more likely presence of such lines in unobscured type-1 sources rather than in obscured sources. This is consistent with the fact that some coronal lines have been recently detected with NIRSpec in the nearby Seyfert 1.5 nucleus of NGC7469 (Bianchin et al. 2023) but not in the highly obscured active nuclei of VV114 (see Appendix B; but see also Speranza et al. 2022; Álvarez-Márquez et al. 2023). The lack of high ionisation lines in AGN sources may reflect an AGN ionising continuum lacking photons below a few keV: this could explain the absence of such line emission in obscured sources (e.g. Rodríguez-Ardila et al. 2011).

High ionisation lines are not detected in the nuclear spectra of Arp 220. However, we note the presence of a bright feature near $\sim 4.488\mu m$, hence close to expected wavelength of the [Mg iv] line ($IP \sim 80$ eV). Previous studies reported the detection of the [Mg iv] line in a few nearby active galaxies alongside other highly ionised species; for instance, Sturm et al. (2002) reported [Mg iv]/[Ar vi] ~ 0.5 in Circinus and NGC1068; Bianchin et al. (2023) obtained [Mg iv]/[Ar vi] ~ 1.5 . Notably, [Ar vi] is not detected in Arp 220. Given its similar IP to [Mg iv] (see Table 4), the observed feature at the expected wavelength of [Mg iv] may involve alternative transitions. For instance, the low-ionisation line Si ($\lambda 4.4855$ in vacuum, $IP \sim 10$ eV) could be responsible of the line features in the Arp 220 spectra.

Figure 5 shows the emission line at the wavelength position of the [Mg iv] in the three spectra of interest: these features are broad ($FWHM \sim 300$ km s $^{-1}$) and blue-shifted ($\Delta V \sim -100$ km s $^{-1}$) with respect to the [Mg iv] expected wavelength (grey solid line at $v = 0$ km/s). Moreover, their peaks are not at the systemic of the SI transition neither. Pereira-Santaella et al. (subm.) show that this feature can be associated with shocked [Mg iv] emission due to supernova explosions. In support of this explanation we note that this line feature is bright at the position of intense clusters in Arp 220, but it is faint in the surroundings of the two nuclei.

In Table 4, we report the main high ionisation lines in the range covered by our NIRSpec spectra; for all but [Mg iv] we report the 3σ upper limits inferred from NIRSpec data. These upper limits, and in particular the [Si vi] one, can be used to compare the NIRSpec measurements with those from the literature. In fact, [Si vi] is detected in the largest number of AGN spectra (Lamperti et al. 2017; den Brok et al. 2022).

Figure 6, top panel, shows the distribution of $L([Si\ vi])$ as a function of the redshift for a sample of nearby active galaxies selected in the hard X-ray band (14-195 keV) from the *Swift*/Burst Alert Telescope (BAT) survey, as part of the BASS sample (Koss et al. 2017; Ricci et al. 2017). We display both [Si vi] detections and 3σ upper limits, alongside the Arp 220 non detections. It is evident that NIRSpec enables us to obtain more stringent up-

per limits compared to previous observations of other systems at $z \sim 0.018$ (by ~ 1 dex).

Figure 6, bottom panel, shows the correlation between intrinsic X-ray and [Si vi] luminosity (e.g. Rodríguez-Ardila et al. 2011; Lamperti et al. 2017) for the same sources. The upper limits for [Si vi] in Arp 220 nuclei are indicated at the intrinsic X-ray (2–10 keV) luminosities of $< 1 \times 10^{42}$ erg s $^{-1}$ (W) and $< 4 \times 10^{41}$ erg s $^{-1}$ (E), computed by Paggi et al. (2017) from the 3σ upper limits on the neutral Fe-K α line. The Arp 220 [Si vi] upper limits are approximately 1 dex below the $L([Si\ vi]) - L_{2-10\ keV}$ relation (dashed magenta line). However, it should be noted that measuring intrinsic X-ray luminosity for highly obscured sources can be highly uncertain, and that the Arp 220 X-ray luminosities are merely upper limits. Consequently, it is possible that the nuclei of Arp 220 may not exhibit notable distinctions from other AGN with undetected [Si vi] reported in the figure, for which the presence of accreting SMBHs is confirmed in the hard X-ray band.

To conclude, there is no obvious highly ionised line emission associated with AGN from either nucleus of Arp 220, despite the many bright H I, He I, H $_2$, and low excitation [Fe II] lines detected at very high signal-to-noise. Moreover, the very stringent upper limits derived from NIRSpec observations cannot be used to discard the presence of AGN in Arp 220 nuclei when we take into account the extremely high nuclear extinction (Sect. 4.3).

Table 4: High ionisation lines

line	λ_{vac} (μm)	IP (eV)	ref	$\log L_{line}$ (erg s $^{-1}$)
(1)	(2)	(3)	(4)	(5)
[S viii]	0.9916	281	L17, C21	<37.0
Cr viii	1.0109	160		<36.9
[Fe xiii]	1.0750	331	L17, C21	<37.0
[Fe xiii]	1.0801	331	L17, C21	<37.0
[S ix]	1.2523	329	B23, C21	<36.9
[Si x]	1.4305	351	C21	–
Ti vi	1.7156	99		<37.3
[S xi]	1.9201	448	L17, C21	<37.1
[Si xi]	1.9327	401	L17, C21	<37.1
[Si vi]	1.9646	167	L17, C21, B23	<37.1
[Al ix]	2.0450	285	C21	<37.1
Sc v	2.3118	73		<37.0
[Ca viii]	2.3211	127	C21, R06	<37.0
[Si vii]	2.4810	205	B23	<37.0
[Si ix]	2.5850	303	S02, L00	<37.1
Al v	2.9050	120		<37.0
[Mg viii]	3.0280	225	S02, B23, L00	<37.0
[Ca iv]	3.2070	51	L00	<36.7
[Al vi]	3.6603	154		<36.9
[Al viii]	3.6900	242		<36.9
[Si ix]	3.9290	303	S02, L00	<37.0
[Ca v]	4.1585	67		<37.0
[Mg iv]	4.4880	80	S02, B23, L00	38.03 ± 0.01 (W) 37.72 ± 0.02 (E)
[Ar vi]	4.5292	75	B23, L00	<37.0

Notes: references of papers reporting the detection of high ionisation lines: Sturm et al. (2002, S02), Lamperti et al. (2017, L17), Bianchin et al. (2023, B23), Cerqueira-Campos et al. (2021, C21), Lutz et al. (2000, L00). [Mg iv] luminosities are reported for both E and W nuclei; for all other high ionisation lines we report 3σ upper limits for the luminosities, assuming $FWHM = 250$ km s $^{-1}$. [Si x] is not covered by NIRSpec observations (it falls in detector gap).

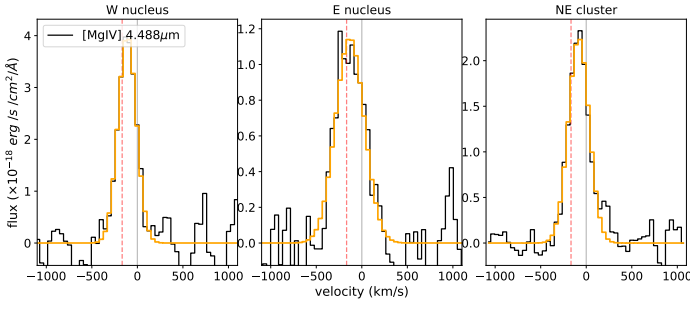


Fig. 5: Continuum-subtracted integrated spectra of the three regions of interest in the vicinity of the $[Mg\text{ IV}]$ $4.488\,\mu\text{m}$. The original spectra (in black) are reported in velocity space. The best-fit emission line profiles are shown in orange. Broad and asymmetric profiles are found in the nuclear spectra. The vertical grey lines mark the zero-velocity as inferred from the narrow component of H I lines; the dashed red lines marks the expected position of the S I line.

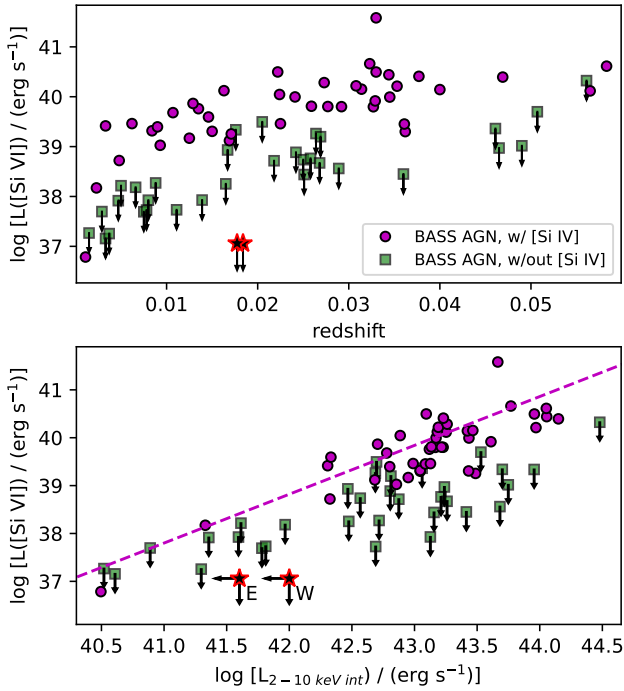


Fig. 6: $[Si\text{ VI}]$ luminosity for Arp 220 and a sample of nearby AGN. (Top panel:) $[Si\text{ VI}]$ luminosity as a function of redshift for the sample of BASS AGN with detected (purple circles) and undetected (green squares) $[Si\text{ VI}]$ line, from Lamperti et al. (2017). Arp 220 measurements are represented by red stars. For sources with undetected $[Si\text{ VI}]$ lines, we provide three-sigma upper limits (illustrated with arrows). (Bottom panel:) $[Si\text{ VI}]$ luminosity as a function of intrinsic X-ray ($2\text{--}10\text{ keV}$) luminosity for the same sources reported in the top panel. The dashed line indicate the linear relation between $L([Si\text{ VI}])$ and $L_{2-10\text{ keV int}}$ obtained by Lamperti et al. (2017, not considering upper limits). X-ray luminosity upper limits for the nuclei of Arp 220 are taken from Paggi et al. (2017).

5.5. Near-infrared emission line diagnostic diagrams

We used the diagnostic diagrams presented by Riffel et al. (2013), Colina et al. (2015), and Calabrò et al. (2023), to investigate the ionisation mechanisms responsible of the emission line ratios observed in the nuclei and the NE cluster. Prior to analysis, all fluxes required for the diagnostics were corrected for dust extinction, using the A_V values reported in Table 1.

According to the diagram presented by Riffel et al. (2013), based on the $H_2\text{ }2.12\mu\text{m}/Bry$ vs. $[Fe\text{ II}]\text{ }1.26\mu\text{m}/Pa\beta$ line ratios, both nuclei and the NE cluster are in the AGN region; the NE cluster has slightly lower line ratios and it is therefore closer to the ‘star-forming’ region of the diagram. In the diagram proposed by Colina et al. (2015), based on the $H_2\text{ }2.12\mu\text{m}/Bry$ vs. $[Fe\text{ II}]\text{ }1.64\mu\text{m}/Bry$, the two nuclei and NE cluster are in the region dominated by AGN and supernovae. Therefore, a similar ionisation mechanism should be present in the W, E, and NE regions of Arp 220 according to both Riffel et al. (2013) and Colina et al. (2015).

We also explored the diagnostic diagram recently proposed by Calabrò et al. (2023), that use combinations of ratios of the $[S\text{ III}]$, $[Fe\text{ II}]$, $[P\text{ II}]$ and $[C\text{ I}]$ lines over hydrogen recombination lines. In all the diagrams, the two nuclei are slightly above the maximum starburst line (by $0.1\text{--}0.5$ dex). The NE clump lies on (or just below) the maximum starburst line. We note that the two nuclei are well above the maximum starburst line in the $[C\text{ I}]/Pa\beta$ diagram, compatible with both AGN and shock ionisations (see Fig. 13 in Calabrò et al. 2023).

In summary, these diagnostics do not allow us to distinguish between supernovae and AGN ionisation mechanisms. More detailed investigations of the flux ratios in the circum-nuclear region of Arp 220 will be presented in a future work.

6. Conclusions

This paper provides an overview of the JWST/NIRSpec IFS observations of Arp 220. It introduces the data reduction, and the continuum and emission line data modelling. It shows the near-infrared spectra of the E and W nuclei, in comparison with that of a bright stellar cluster at $\sim 0.4''$ (0.15 kpc) north-east from the E nucleus. These spectra are extracted using circular apertures of radius 55 pc ($0.15''$) for each region. In the following, we summarise our main findings.

We identify broadening and multiple kinematic components in H I, H_2 and $[Fe\text{ II}]$ lines caused by outflows (Fig. 3). The emission line features show maximum velocities of up to $\sim 550\text{ km s}^{-1}$ in the nuclear spectra. Even higher velocities ($\sim 900\text{ km s}^{-1}$) are detected in the off-nuclear regions (Fig. 4). However, they do not conclusively represent a direct evidence of AGN activity. A companion paper will report the spatially resolved gas kinematics, and the outflow energetics will be used to test the theoretical predictions for both starburst- and AGN-driven winds (Ulivi et al., in prep.).

High ionisation lines associated with AGN activity are not detected in the nuclear spectra of Arp 220. We observe the presence of bright $[Mg\text{ IV}]\text{ }4.488\,\mu\text{m}$ lines (80 eV) in the two nuclear spectra and the NE stellar cluster (Fig. 5). However, no other high ionisation lines are detected; in particular the $[Ar\text{ VI}]\text{ }4.529\,\mu\text{m}$ line, which has an IP and wavelength close to those of $[Mg\text{ IV}]$, is not detected. The $[Mg\text{ IV}]$ lines are broader (FWHM $\sim 300\text{ km s}^{-1}$) and blue-shifted ($\Delta V \sim -100\text{ km s}^{-1}$) compared to those of the H I lines; moreover, $[Mg\text{ IV}]$ is bright at the position of clusters, but it is faint in the surroundings of the two nuclei. These arguments suggest that this emission line is

not produced by an AGN, but rather due to stellar activity. This result is in line with recent findings of Pereira-Santaella et al. (subm.), who recently reported the presence of [Mg iv] in other nearby ULIRGs not hosting accreting SMBHs, with kinematic properties similar to those in Arp 220; they also provided grids of photoionization and shock models to determine the conditions where [Mg iv] originates, concluding that shocks by supernova explosions can explain the observed [Mg iv] lines.

The luminosity upper limits inferred for the high ionisation (IP = 167 eV) [Si vi] emission line at the position of the Arp 220 nuclei are ~ 1 dex below the $L([\text{Si vi}]) - L_{2-10 \text{ keV, int}}$ observed for X-ray AGN (Rodríguez-Ardila et al. 2011; Lamperti et al. 2017), but still broadly consistent with other sources hosting accreting SMBHs but missing [Si vi] emission (Fig. 6).

We also report the presence of high excitation ^{12}CO gas transitions (up to $J_{\text{low}} = 23$) in the Arp 220 nuclei (Fig. B.6), possibly due to AGN activity (e.g. González-Alfonso et al. 2023). A companion paper (Buiten et al., in prep.) will provide detailed modelling of CO gas conditions to assess which mechanism among star formation and AGN contributes to the observed high excitation CO lines.

To conclude, an unambiguous identification of the presence of AGN in the Arp 220 system remains elusive. At the same time, we cannot exclude the presence of accreting SMBHs, because of the extremely high extinction measured at the position of the two nuclei, with recombination lines-based $A_V \sim 11 - 14$. NIR-Spec observations may only probe the outer gaseous layers, and the total extinction towards the core of the Arp 220 nuclear regions could be much higher (see e.g. Haas et al. 2001; Sakamoto et al. 2021a). This could explain the absence of highly ionised gas transitions, as also reported in previous works on obscured AGN (e.g. Rodríguez-Ardila et al. 2011; Lamperti et al. 2017).

Acknowledgements

We are grateful to Paul van der Werf, Victorine Buiten, and Angèle Taillard for discussing various aspects of this work

MP, SA, and BRP acknowledge support from the research project PID2021-127718NB-I00 of the Spanish Ministry of Science and Innovation/State Agency of Research (MCIN/AEI/10.13039/501100011033). IL acknowledges support from PID2022-140483NB-C22 funded by AEI 10.13039/501100011033 and BDC 20221289 funded by MCIN by the Recovery, Transformation and Resilience Plan from the Spanish State, and by NextGenerationEU from the European Union through the Recovery and Resilience Facility. MPS acknowledges support from grant RYC2021-033094-I funded by MICIU/AEI/10.13039/501100011033 and the European Union NextGenerationEU/PRTR. RM acknowledges support by the Science and Technology Facilities Council (STFC), by the ERC Advanced Grant 695671 “QUENCH”, and by the UKRI Frontier Research grant RISEandFALL; RM is further supported by a research professorship from the Royal Society. GC, MP, and LU acknowledge the support of the INAF Large Grant 2022 “The metal circle: a new sharp view of the baryon cycle up to Cosmic Dawn with the latest generation IFU facilities”.

References

Álvarez-Márquez, J., Labiano, A., Guillard, P., et al. 2023, A&A, 672, A108
 Armus, L., Charmandaris, V., Bernard-Salas, J., et al. 2007, ApJ, 656, 148
 Arp, H. 1966, ApJS, 14, 1
 Arribas, S., Colina, L., & Clements, D. 2001, ApJ, 560, 160
 Baan, W. A. & Haschick, A. D. 1995, ApJ, 454, 745
 Baba, S., Imanishi, M., Izumi, T., et al. 2022, ApJ, 928, 184

Barcos-Muñoz, L., Leroy, A. K., Evans, A. S., et al. 2015, ApJ, 799, 10
 Bennett, C. L., Larson, D., Weiland, J. L., & Hinshaw, G. 2014, ApJ, 794, 135
 Bianchin, M., U. V., Song, Y., et al. 2023, arXiv e-prints, arXiv:2308.00209
 Böker, T., Arribas, S., Lützgendorf, N., et al. 2022, A&A, 661, A82
 Böker, T., Beck, T. L., Birkmann, S. M., et al. 2023, PASP, 135, 038001
 Buiten, V. A., van der Werf, P. P., Viti, S., et al. 2023, arXiv e-prints, arXiv:2312.01945
 Calabrò, A., Pentericci, L., Feltre, A., et al. 2023, A&A, 679, A80
 Cappellari, M. 2017, MNRAS, 466, 798
 Cardelli, J. A., Clayton, G. C., & Mathis, J. S. 1989, ApJ, 345, 245
 Cerqueira-Campos, F. C., Rodríguez-Ardila, A., Riffel, R., et al. 2021, MNRAS, 500, 2666
 Chabrier, G. 2003, PASP, 115, 763
 Chandar, R., Caputo, M., Linden, S., et al. 2023, ApJ, 943, 142
 Colina, L., Arribas, S., & Clements, D. 2004, ApJ, 602, 181
 Colina, L., Piqueras López, J., Arribas, S., et al. 2015, A&A, 578, A48
 Cresci, G., Tozzi, G., Perna, M., et al. 2023, arXiv e-prints, arXiv:2301.11060
 Davies, R. L., Förster Schreiber, N. M., Genzel, R., et al. 2021, ApJ, 909, 78
 Davis, C. J., Cervantes, B., Nisini, B., et al. 2011, A&A, 528, A3
 den Brok, J. S., Koss, M. J., Trakhtenbrot, B., et al. 2022, ApJS, 261, 7
 D’Eugenio, F., Perez-Gonzalez, P., Maiolino, R., et al. 2023, arXiv e-prints, arXiv:2308.06317
 Donnan, F. R., García-Bernete, I., Rigopoulou, D., et al. 2024, MNRAS[arXiv:2402.17479]
 Emonts, B. H. C., Colina, L., Piqueras-López, J., et al. 2017, A&A, 607, A116
 Engel, H., Davies, R. I., Genzel, R., et al. 2011, ApJ, 729, 58
 Eriksen, K. A., Arnett, D., McCarthy, D. W., & Young, P. 2009, ApJ, 697, 29
 Fluetsch, A., Maiolino, R., Carniani, S., et al. 2021, MNRAS, 505, 5753
 Förster Schreiber, N. M., Übler, H., Davies, R. L., et al. 2019, ApJ, 875, 21
 García-Bernete, I., Pereira-Santaella, M., González-Alfonso, E., et al. 2024, A&A, 682, L5
 Gibb, E. L., Whittet, D. C. B., Boogert, A. C. A., & Tielens, A. G. G. M. 2004, ApJS, 151, 35
 Giménez-Arteaga, C., Brammer, G. B., Marchesini, D., et al. 2022, ApJS, 263, 17
 González-Alfonso, E., García-Bernete, I., Pereira-Santaella, M., et al. 2023, arXiv e-prints, arXiv:2312.04914
 Gustafsson, B., Edvardsson, B., Eriksson, K., et al. 2008, A&A, 486, 951
 Haas, M., Klaas, U., Müller, S. A. H., Chini, R., & Coulson, I. 2001, A&A, 367, L9
 Isobe, Y., Ouchi, M., Nakajima, K., et al. 2023, ApJ, 956, 139
 Jakobsen, P., Ferruit, P., de Oliveira, C. A., et al. 2022, A&A, 661, A80
 Kennicutt, R. C. & Evans, N. J. 2012, ARA&A, 50, 531
 Kim, J. H., Im, M., Lee, H. M., et al. 2012, ApJ, 760, 120
 Koo, B.-C., Raymond, J. C., & Kim, H.-J. 2016, Journal of Korean Astronomical Society, 49, 109
 Koss, M., Trakhtenbrot, B., Ricci, C., et al. 2017, ApJ, 850, 74
 Lamperti, I., Koss, M., Trakhtenbrot, B., et al. 2017, MNRAS, 467, 540
 Lamperti, I., Pereira-Santaella, M., Perna, M., et al. 2022, A&A, 668, A45
 Law, D. D., Morrison, J. E., Argyriou, I., et al. 2023, AJ, 166, 45
 Lee, Y.-H., Koo, B.-C., Moon, D.-S., Burton, M. G., & Lee, J.-J. 2017, ApJ, 837, 118
 Lockhart, K. E., Kewley, L. J., Lu, J. R., et al. 2015, ApJ, 810, 149
 Lutz, D., Sturm, E., Genzel, R., et al. 2000, ApJ, 536, 697
 May, D. & Steiner, J. E. 2017, MNRAS, 469, 994
 McDowell, J. C., Clements, D. L., Lamb, S. A., et al. 2003, ApJ, 591, 154
 Moorwood, A. F. M., Marconi, A., van der Werf, P. P., & Oliva, E. 1997, Ap&SS, 248, 113
 Nardini, E., Risaliti, G., Watabe, Y., Salvati, M., & Sani, E. 2010, MNRAS, 405, 2505
 Oliva, E., Origlia, L., Kotilainen, J. K., & Moorwood, A. F. M. 1995, A&A, 301, 55
 Oliva, E., Salvati, M., Moorwood, A. F. M., & Marconi, A. 1994, A&A, 288, 457
 Osterbrock, D. E. & Ferland, G. J. 2006, Astrophysics of gaseous nebulae and active galactic nuclei (University Science Books)
 Paggi, A., Fabbiano, G., Risaliti, G., et al. 2017, ApJ, 841, 44
 Pereira-Santaella, M., Colina, L., García-Burillo, S., et al. 2021, A&A, 651, A42
 Pereira-Santaella, M., González-Alfonso, E., García-Bernete, I., García-Burillo, S., & Rigopoulou, D. 2024, A&A, 681, A117
 Perna, M., Arribas, S., Catalán-Torrecilla, C., et al. 2020, A&A, 643, A139
 Perna, M., Arribas, S., Marshall, M., et al. 2023, A&A, 679, A89
 Perna, M., Arribas, S., Pereira Santaella, M., et al. 2021, A&A, 646, A101
 Perna, M., Brusa, M., Cresci, G., et al. 2015, A&A, 574, A82
 Perna, M., Lanzuisi, G., Brusa, M., Cresci, G., & Mignoli, M. 2017, A&A, 606, A96
 Piqueras López, J., Colina, L., Arribas, S., Pereira-Santaella, M., & Alonso-Herrero, A. 2016, A&A, 590, A67
 Ralchenko, Y. 2005, Memorie della Societa Astronomica Italiana Supplementi, 8, 96

- Reddy, N. A., Sanders, R. L., Shapley, A. E., et al. 2023, *ApJ*, 951, 56
- Ricci, C., Trakhtenbrot, B., Koss, M. J., et al. 2017, *ApJS*, 233, 17
- Rich, J., Aalto, S., Evans, A. S., et al. 2023, *ApJ*, 944, L50
- Riffel, R., Rodríguez-Ardila, A., Aleman, I., et al. 2013, *MNRAS*, 430, 2002
- Riffel, R., Rodríguez-Ardila, A., Brotherton, M. S., et al. 2019, *MNRAS*, 486, 3228
- Riffel, R. A., Vale, T. B., Storchi-Bergmann, T., & McGregor, P. J. 2014, *MNRAS*, 442, 656
- Rodríguez-Ardila, A., Prieto, M. A., Portilla, J. G., & Tejeiro, J. M. 2011, *ApJ*, 743, 100
- Rodríguez Del Pino, B., Perna, M., Arribas, S., et al. 2023, *arXiv e-prints*, arXiv:2309.14431
- Rothman, L. S. 2021, *Nature Reviews Physics*, 3, 302
- Sakamoto, K., González-Alfonso, E., Martín, S., et al. 2021a, *ApJ*, 923, 206
- Sakamoto, K., Martín, S., Wilner, D. J., et al. 2021b, *ApJ*, 923, 240
- Schwarz, U. J. 1978, *A&A*, 65, 345
- Scoville, N., Aussel, H., Brusa, M., et al. 2007, *ApJS*, 172, 1
- Scoville, N., Murchikova, L., Walter, F., et al. 2017, *ApJ*, 836, 66
- Scoville, N. Z., Evans, A. S., Dinshaw, N., et al. 1998, *ApJ*, 492, L107
- Shimakawa, R., Kodama, T., Steidel, C. C., et al. 2015, *MNRAS*, 451, 1284
- Speranza, G., Ramos Almeida, C., Acosta-Pulido, J. A., et al. 2022, *A&A*, 665, A55
- Sturm, E., Lutz, D., Verma, A., et al. 2002, *A&A*, 393, 821
- Teng, S. H., Rigby, J. R., Stern, D., et al. 2015, *ApJ*, 814, 56
- Ueda, J., Michiyama, T., Iono, D., Miyamoto, Y., & Saito, T. 2022, *PASJ*, 74, 407
- Ulivi et al., . in prep., —, —,
- Varenus, E., Conway, J. E., Batejat, F., et al. 2019, *A&A*, 623, A173
- Varenus, E., Conway, J. E., Martí-Vidal, I., et al. 2016, *A&A*, 593, A86
- Vazdekis, A., Koleva, M., Ricciardelli, E., Röck, B., & Falcón-Barroso, J. 2016, *MNRAS*, 463, 3409
- Vero, K., Trager, S. C., Peletier, R. F., et al. 2022, *A&A*, 660, A34
- Villar Martín, M., Castro-Rodríguez, N., Pereira Santaella, M., et al. 2023, *A&A*, 673, A25
- Wheeler, J., Glenn, J., Rangwala, N., & Fyhrie, A. 2020, *ApJ*, 896, 43
- Yoast-Hull, T. M., Gallagher, John S., I., Aalto, S., & Varenus, E. 2017, *MNRAS*, 469, L89
- Yoast-Hull, T. M. & Murray, N. 2019, *MNRAS*, 484, 3665

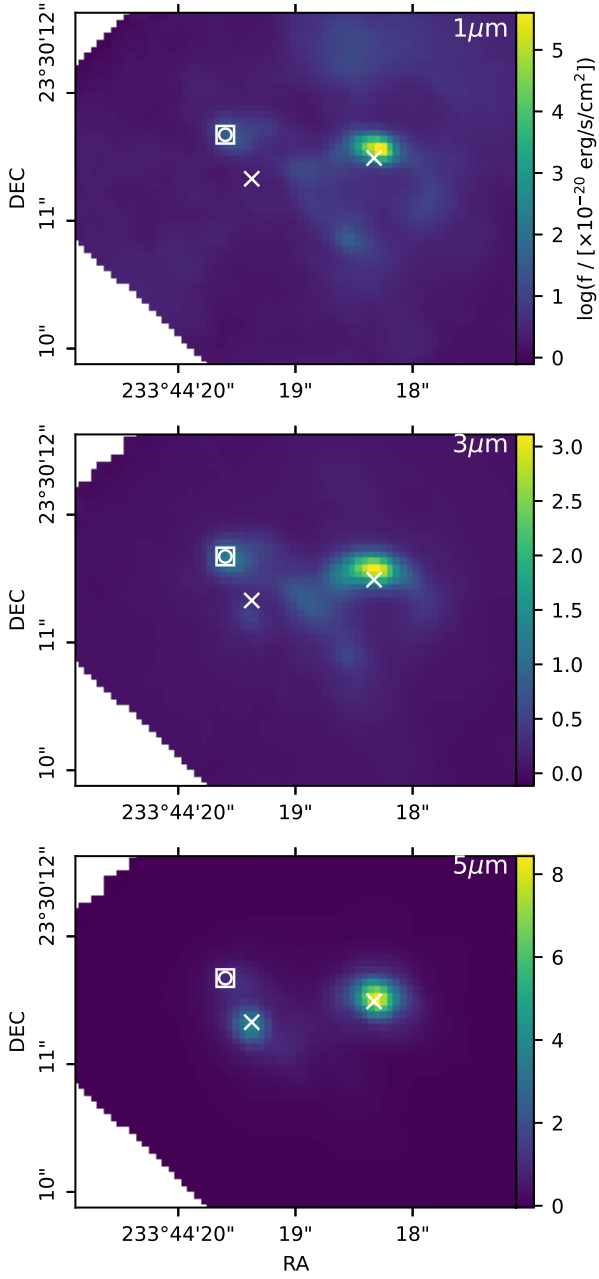


Fig. A.1: *NIRSpec* narrow-band images tracing the continuum emission at $\sim 1\mu\text{m}$ (top), $3\mu\text{m}$ (centre) and $5\mu\text{m}$ (bottom). The position of the W and E nuclei are marked with x symbols; the box-circle symbol marks the position of a bright cluster (see also Fig. 1)

Appendix A: *NIRSpec* narrow-band images

Appendix B: Integrated spectra

Appendix C: Arp 220 emission line list (band2 and band3 cubes)

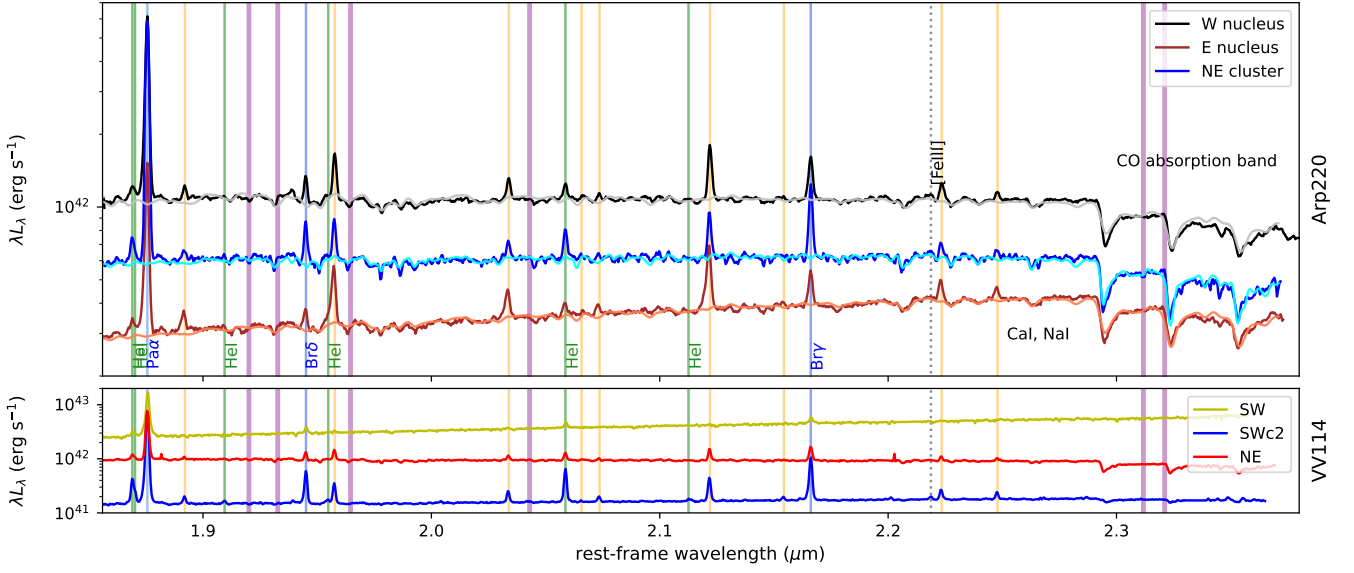


Fig. B.3: 1.85 – 2.40 μm portion on the spectra of the Arp 220 and VV114 nuclear regions. See B.1 for further details.

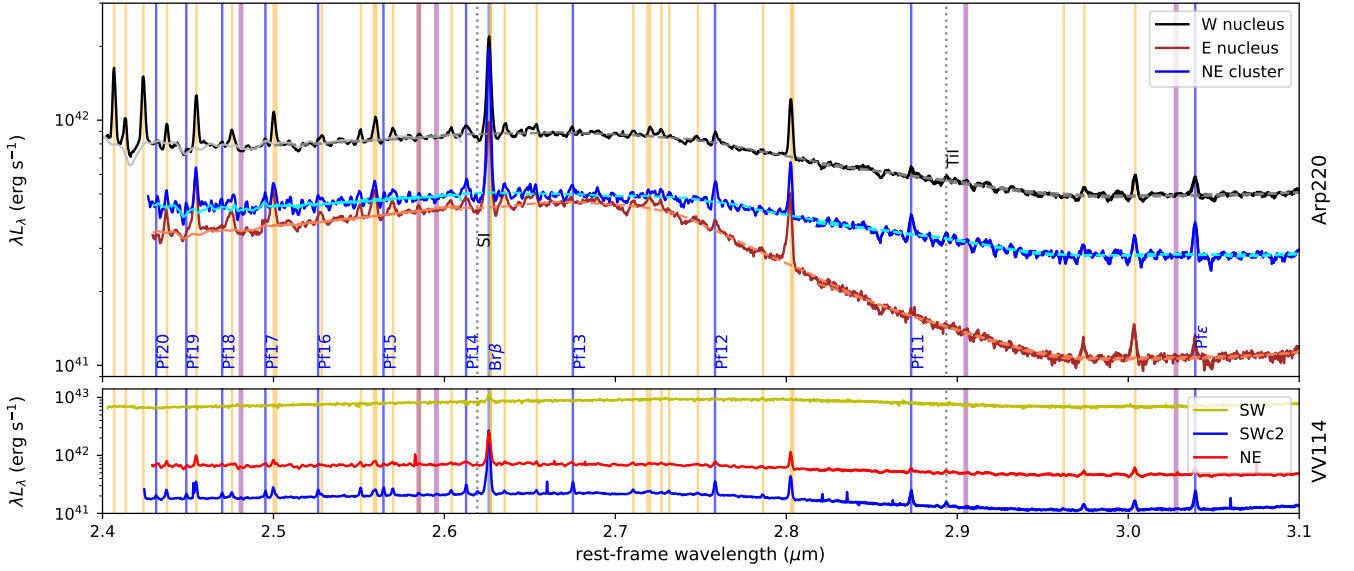


Fig. B.4: 2.4 – 3.1 μm portion on the spectra of the Arp 220 and VV114 nuclear regions. The pseudo-continuum described in Sect. 3.3 are shown with dashed curves. See B.1 for further details.

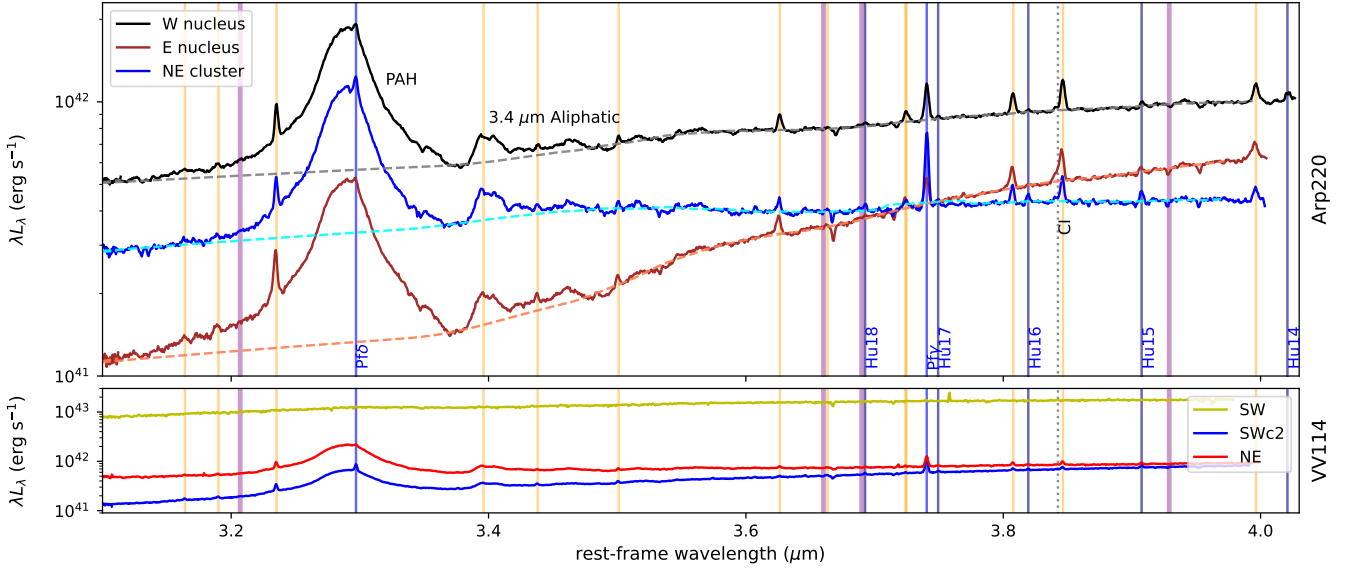


Fig. B.5: 3.1 – 4.0 μm portion on the spectra of the Arp 220 and VV114 nuclear regions. See B.1 for further details.

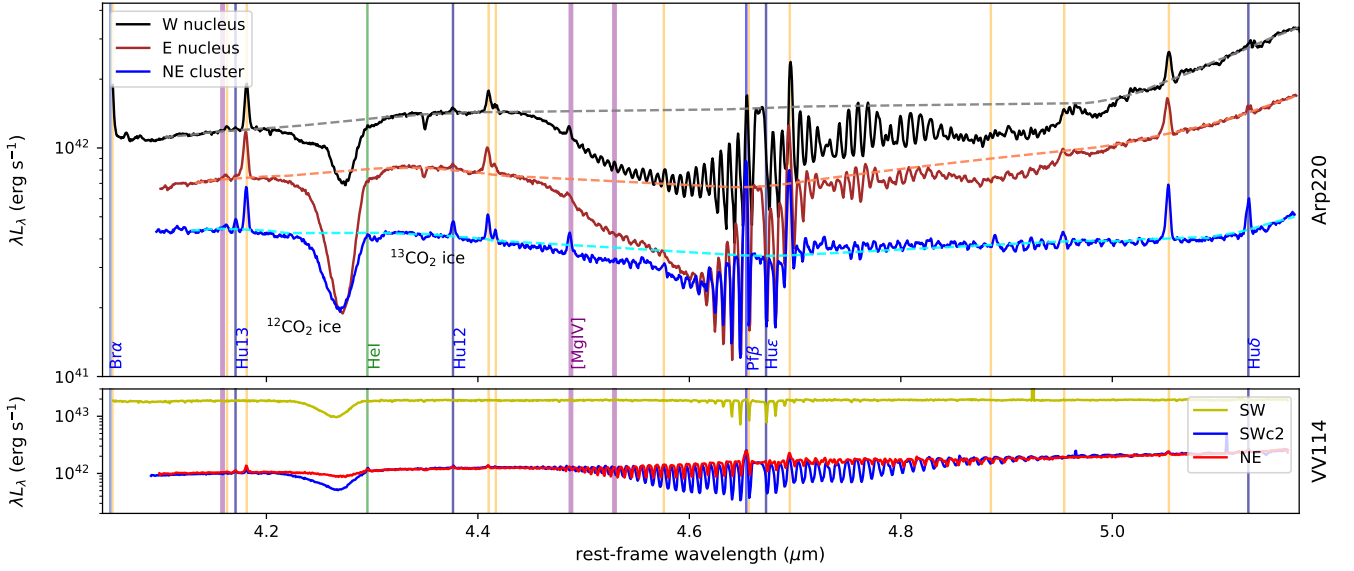


Fig. B.6: 4.1 – 5.2 μm portion on the spectra of Arp 220 and VV114 nuclear regions. The E and W nuclei show ^{12}CO ro-vibrational lines up to $J_{\text{low}} = 23$ (close to the [Mg IV] line transition, at $\sim 4.48 \mu\text{m}$, and at $\sim 4.88 \mu\text{m}$; see e.g. [González-Alfonso et al. 2023](#)). Detailed modelling of the CO transitions will be presented in Buiten et al., in prep.. See B.1 for further details.

Table C.1: Arp 220 emission line list in the W and E nuclei, and NE cluster (band2 spectra)

line	λ_{vac} (μm)	f_W ($10^{-18} \text{ erg s}^{-1} \text{ cm}^{-2}$)	f_E ($10^{-18} \text{ erg s}^{-1} \text{ cm}^{-2}$)	f_{NE} ($10^{-18} \text{ erg s}^{-1} \text{ cm}^{-2}$)
He I	1.869044	273.0 ^{+6.8} _{-3.3}	62.3 ^{+4.7} _{-2.8}	193.0 ^{+5.0} _{-3.9}
He I	1.870234	112.0 ^{+3.8} _{-3.5}	35.1 ^{+4.6} _{-2.9}	36.7 ^{+6.3} _{-3.3}
Pa α	1.875627	7260.0 ^{+5.4} _{-2.9}	1510.0 ^{+2.1} _{-2.6}	6390.0 ^{+5.8} _{-4.0}
H ₂	1.892094	253.0 ^{+5.1} _{-5.0}	77.7 ^{+32.3} _{-11.9}	85.6 ^{+0.8} _{-1.0}
Br δ	1.945095	455.0 ^{+4.5} _{-5.7}	77.2 ^{+4.5} _{-2.8}	334.0 ^{+6.6} _{-3.2}
He I	1.954840	27.2 ^{+3.1} _{-1.8}	46.6 ^{+2.7} _{-3.1}	30.5 ^{+2.1} _{-2.7}
H ₂	1.957722	659.0 ^{+6.9} _{-3.4}	243.0 ^{+86.2} _{-45.6}	278.0 ^{+8.8} _{-3.3}
H ₂	2.033927	268.0 ^{+3.4} _{-3.4}	149.0 ^{+5.1} _{-3.4}	116.0 ^{+3.8} _{-3.1}
He I	2.058600	247.0 ^{+1.4} _{-1.3}	62.6 ^{+1.3} _{-0.6}	215.0 ^{+2.2} _{-1.1}
H ₂	2.065756	81.7 ^{+0.5} _{-0.7}	28.9 ^{+4.7} _{-2.0}	33.3 ^{+4.2} _{-4.2}
H ₂	2.073655	126.0 ^{+3.0} _{-4.6}	69.6 ^{+4.0} _{-3.4}	59.1 ^{+3.1} _{-4.3}
H ₂	2.122011	901.0 ^{+7.8} _{-5.1}	427.0 ^{+6.0} _{-3.6}	345.0 ^{+6.6} _{-5.4}
Br γ	2.166129	762.0 ^{+5.5} _{-4.1}	156.0 ^{+9.2} _{-4.9}	686.0 ^{+5.9} _{-2.8}
H ₂	2.223475	263.0 ^{+3.4} _{-5.5}	123.0 ^{+4.2} _{-4.1}	100.0 ^{+5.3} _{-2.8}
H ₂	2.247903	147.0 ^{+2.4} _{-3.3}	76.2 ^{+3.0} _{-3.5}	69.6 ^{+1.0} _{-0.9}
H ₂	2.406793	1010.0 ^{+9.7} _{-5.6}	—	—
H ₂	2.413640	402.0 ^{+8.0} _{-3.9}	—	—
H ₂	2.423932	940.0 ^{+9.2} _{-4.7}	—	—
H ₂	2.454956	633 ^{+5.4} _{-3.0}	375 ^{+5.0} _{-4.4}	223 ^{+5.3} _{-3.8}
H ₂	2.475765	173.0 ^{+3.1} _{-1.8}	124.0 ^{+3.0} _{-4.0}	62.4 ^{+1.0} _{-0.8}
H ₂	2.500174	332.0 ^{+4.0} _{-2.1}	207.0 ^{+4.4} _{-3.1}	106.0 ^{+4.9} _{-2.6}
H ₂	2.501650	50.9 ^{+3.0} _{-2.4}	19.4 ^{+5.0} _{-2.7}	39.0 ^{+2.9} _{-3.1}
H ₂	2.528247	87.8 ^{+0.6} _{-1.2}	58.6 ^{+3.9} _{-1.7}	34.6 ^{+3.9} _{-1.7}
H ₂	2.551198	103.0 ^{+5.0} _{-1.6}	72.7 ^{+4.1} _{-1.7}	33.8 ^{+4.1} _{-2.9}
H ₂	2.558725	96.0 ^{+4.6} _{-2.7}	61.4 ^{+5.3} _{-3.7}	54.8 ^{+2.2} _{-1.7}
H ₂	2.560064	193.0 ^{+3.3} _{-2.6}	121.0 ^{+5.4} _{-2.6}	48.9 ^{+3.0} _{-2.1}
H ₂	2.570043	124.0 ^{+4.5} _{-2.7}	89.6 ^{+3.3} _{-2.7}	44.8 ^{+2.8} _{-2.5}
H ₂	2.585185	31.3 ^{+2.5} _{-1.6}	20.1 ^{+4.1} _{-3.6}	1.76 ^{+3.6} _{-0.7}
H ₂	2.604197	66.5 ^{+3.7} _{-2.4}	46.1 ^{+4.8} _{-3.0}	25.5 ^{+4.1} _{-3.1}
Pf 14	2.612655	121.0 ^{+0.3} _{-0.1}	70.9 ^{+4.7} _{-2.3}	84.6 ^{+6.0} _{-2.2}
Br β	2.625878	1840.0 ^{+6.2} _{-3.9}	749.0 ^{+6.5} _{-4.4}	1610.0 ^{+5.9} _{-4.8}
H ₂	2.635329	103.0 ^{+2.9} _{-3.0}	89.8 ^{+4.0} _{-3.2}	45.8 ^{+3.5} _{-3.8}
H ₂	2.654084	80.5 ^{+3.1} _{-4.3}	65.1 ^{+3.7} _{-2.6}	24.2 ^{+5.8} _{-1.6}
Pf 13	2.675139	58.9 ^{+5.1} _{-6.0}	17.1 ^{+4.0} _{-3.5}	51.4 ^{+6.4} _{-2.5}
H ₂	2.710478	48.9 ^{+0.4} _{-3.0}	19.7 ^{+5.4} _{-1.4}	12.7 ^{+3.6} _{-2.7}
H ₂	2.718847	1.19 ^{+0.006} _{-0.004}	2.29 ^{+5.5} _{-0.74}	4.55 ^{+1.6} _{-2.2}
H ₂	2.720371	103.0 ^{+2.4} _{-0.94}	81.3 ^{+4.9} _{-2.2}	26.4 ^{+3.7} _{-1.9}
H ₂	2.726984	87.1 ^{+1.0} _{-2.6}	59.6 ^{+3.4} _{-1.5}	33.2 ^{+3.0} _{-1.5}
H ₂	2.731438	17.3 ^{+5.4} _{-2.6}	10.0 ^{+2.9} _{-2.1}	14.8 ^{+3.6} _{-1.6}
H ₂	2.748299	32.0 ^{+4.0} _{-3.4}	20.3 ^{+3.4} _{-2.8}	11.2 ^{+2.5} _{-3.9}
Pf 12	2.758276	110.0 ^{+6.3} _{-1.9}	48.0 ^{+4.6} _{-2.7}	109.0 ^{+4.3} _{-3.0}
H ₂	2.786396	12.5 ^{+4.4} _{-2.0}	13.6 ^{+4.0} _{-2.8}	6.99 ^{+3.7} _{-2.4}
H ₂	2.802750	601.0 ^{+3.6} _{-3.8}	313.0 ^{+4.3} _{-1.3}	244.0 ^{+3.2} _{-1.7}
H ₂	2.804052	1.25 ^{+0.007} _{-0.004}	1.41 ^{+0.03} _{-0.02}	1.08 ^{+0.01} _{-0.01}
Pf 11	2.873004	58.7 ^{+5.7} _{-2.4}	8.35 ^{+3.2} _{-1.8}	74.4 ^{+3.5} _{-2.6}
H ₂	2.974311	54.0 ^{+2.5} _{-2.5}	22.7 ^{+2.7} _{-2.4}	27.2 ^{+2.9} _{-2.2}
H ₂	3.004118	132.0 ^{+3.7} _{-2.8}	48.5 ^{+2.7} _{-2.2}	53.5 ^{+3.5} _{-1.9}
Pf ϵ	3.039211	128.0 ^{+7.3} _{-2.9}	21.3 ^{+3.1} _{-4.1}	110.0 ^{+6.6} _{-3.3}

Notes: This list comprises all emission lines detected in band2; see Tables 2 and C.2 for those in band1 and band3, respectively. The reported fluxes are obtained from single Gaussian fits, without dust- and aperture-corrections.

Table C.2: Arp 220 emission line list in the W and E nuclei, and NE cluster (band3 spectra)

line	λ_{vac} (μm)	f_W ($10^{-18} \text{ erg s}^{-1} \text{ cm}^{-2}$)	f_E ($10^{-18} \text{ erg s}^{-1} \text{ cm}^{-2}$)	f_{NE} ($10^{-18} \text{ erg s}^{-1} \text{ cm}^{-2}$)
H ₂	3.164034	$15.2^{+2.1}_{-2.4}$	$8.13^{+2.0}_{-1.6}$	$13.4^{+3.0}_{-2.3}$
H ₂	3.190077	$28.2^{+2.4}_{-1.8}$	$13.4^{+2.6}_{-1.4}$	$11.9^{+2.6}_{-2.2}$
H ₂	3.235257	$310.0^{+5.3}_{-2.2}$	$117.0^{+2.8}_{-1.1}$	$117.0^{+2.2}_{-1.7}$
Pf δ	3.297001	$409.0^{+0.8}_{-0.6}$	$74.3^{+5.1}_{-3.2}$	$293.0^{+1.7}_{-1.3}$
H ₂	3.626469	$152.0^{+3.5}_{-2.7}$	$70.4^{+2.5}_{-1.8}$	$47.6^{+4.1}_{-1.4}$
H ₂	3.663464	$23.2^{+2.8}_{-2.3}$	$29.0^{+1.9}_{-1.0}$	$12.2^{+5.2}_{-1.0}$
Hu 18	3.692642	$30.2^{+2.6}_{-1.6}$	$9.63^{+2.1}_{-0.8}$	$23.5^{+2.8}_{-1.9}$
H ₂	3.723999	$5.49^{+4.8}_{-4.7}$	$0.898^{+0.021}_{-0.006}$	$3.75^{+4.8}_{-2.2}$
H ₂	3.724736	$110.0^{+4.7}_{-4.0}$	$59.3^{+2.6}_{-1.2}$	$30.4^{+3.8}_{-4.3}$
Pf γ	3.740568	$414.0^{+3.8}_{-3.3}$	$111.0^{+4.7}_{-3.5}$	$398.0^{+2.6}_{-1.7}$
Hu 17	3.749402	$12.6^{+3.2}_{-2.1}$	$2.87^{+2.9}_{-2.0}$	$19.5^{+3.1}_{-2.4}$
H ₂	3.807736	$215.0^{+2.1}_{-2.7}$	$93.5^{+3.1}_{-16.9}$	$70.6^{+2.2}_{-1.6}$
Hu 16	3.819460	$16.9^{+3.3}_{-2.0}$	$3.96^{+3.2}_{-2.1}$	$25.4^{+2.7}_{-2.3}$
C I (?)	3.841473	$24.2^{+1.7}_{-0.9}$	$26^{+2.4}_{-1.6}$	$13.3^{+1.9}_{-1.3}$
H ₂	3.846434	$349.0^{+3.1}_{-2.6}$	$186.0^{+2.9}_{-2.4}$	$99.6^{+3.4}_{-1.2}$
Hu 15	3.907557	$41.7^{+4.3}_{-2.5}$	$23.6^{+3.2}_{-1.7}$	$36.7^{+2.7}_{-1.8}$
H ₂	4.162772	$63.1^{+5.4}_{-2.5}$	$47.0^{+3.5}_{-2.2}$	$24.1^{+1.7}_{-1.5}$
Hu 13	4.170803	$26.8^{+3.6}_{-3.6}$	$77.4^{+18.8}_{-10.3}$	$45.0^{+3.4}_{-1.9}$
H ₂	4.181426	$941.0^{+5.4}_{-2.6}$	$580.0^{+4.8}_{-3.3}$	$248.0^{+3.0}_{-1.7}$
Hu 12	4.376464	$78.1^{+3.7}_{-3.0}$	$33.0^{+3.4}_{-1.6}$	$59.5^{+3.4}_{-1.2}$
H ₂	4.410159	$454.0^{+2.1}_{-2.0}$	$292.0^{+4.9}_{-1.3}$	$117.0^{+2.2}_{-1.2}$
H ₂	4.416979	$142.0^{+2.8}_{-1.8}$	$71.2^{+3.7}_{-2.3}$	$41.4^{+1.4}_{-1.0}$
H ₂	5.053536	$972.0^{+7.1}_{-4.8}$	$644.0^{+5.7}_{-5.8}$	$289.0^{+4.5}_{-1.9}$
Hu δ	5.128669	$148.0^{+6.7}_{-3.6}$	$120.0^{+5.3}_{-3.5}$	$183.0^{+2.1}_{-2.7}$

Notes: This list comprises all emission lines detected in band3; see also Tables 2 and C.1 for those in band1 and band2, respectively. The reported fluxes are obtained from single Gaussian fits, without dust- and aperture-corrections.